New Xenon Gas Polarizer with application to Magnetic Resonance Imaging

---

A Dissertation

Presented to

the faculty of the School of Engineering and Applied Science

University of Virginia

In Partial Fulfillment

of the requirements for the Degree

of Doctor of Philosophy in Biomedical Engineering

by

Hsuan-Tsung James Wang

January 2007

Approval Sheet

The dissertation is submitted in partial fulfillment of the

requirements for the degree of

Doctor of Philosophy in Biomedical Engineering

_____

Hsuan-Tsung J. Wang, Author

This dissertation has been read and approved by the examining committee:

_____

Dr. Craig H. Meyer, Chair

_____

Dr. Gordon D. Cates, Dissertation Advisor

_____

Dr. James R. Brookeman

_____

Dr. John P. Mugler, III

_____

Dr. Mark B. Williams

Accepted for the School of Engineering and Applied Science:

_____

Dean, School of Engineering and Applied Science

January 2007

Acknowledgements

I present deepest thanks to my advisor, Dr. Gordon D. Cates, for his invaluable help, guidance, and encouragement in this study. He shared with me a physicist's perspective and approach to an unsolved problem. I would like to thank Dr. William A. Tobias, for teaching me gas- and vacuum-system technology, many discussions and much help throughout these years; Jaideep Singh for help and discussions on physics, optics, and Labview programming; Scott Rohrbaugh for his many suggestions, discussions and the electromagnet shimming; Dr. Vladimir Nelyubin for laboratory help; and Michael Carr for aiding the gas panel work and the xenon gas diffusion study.

Dr. Stuart Berr generously gave us his superconducting magnet and allowed us to use his laboratory space for two years. Jack Roy helped me in some facility-related problems. I am grateful to Dr. James R. Brookeman, Dr. John P. Mugler III, Dr. Mark B. Williams, and Dr. Craig H. Meyer for their invaluable advices; Dr. Jaime F. Mata for his discussions on xenon gas polarizer and many rabbit lung MRI imaging experiments; and Dr. Wilson Miller for collaborations and MRI lessons.

I appreciate William Shoup and Michael Souza for their help and excellent glass work. I thank Dr. Thomas Gentile, Earl Babcock, and Dr. Thad Walker for their helps and discussions on external-cavity line-narrowing diode laser technology.

This study was supported by funds of the Medical School, University of Virginia.

Closer to home, the most thanks to my father Der-Her, mother I-Chin, my wife Yu-Li for her long term support and dedication; also my daughter Tina (Western Albemarle Junior Varsity Soccer, 2006), Anita (SOCA U13 Express) and son Edward (SOCA U12 Metro). Their soccer games encouraged and inspired me on the spin physics.

Table of contents:

Abstract

This thesis describes the development and construction of a new xenon gas polarizer. The main motivation was to investigate methods to increase the xenon polarization and to promote its application in magnetic resonance imaging (MRI) and other biomedical research.

The polarizer is based on the technique of spin-exchange optical pumping. Since xenon is very depolarizing to rubidium spins, dilute xenon gas is used in the pumping chamber. Laser polarized xenon gas is accumulated in a separate liquid nitrogen cold bath. At the end, the xenon ice is thawed-out and applied for animal or human lung imaging.

Two nuclear magnetic resonance (NMR) instruments were built to monitor xenon polarizations. Both water (^{1}H) and enriched ^{129}Xe phantoms were used for calibration.

The laser system developed for the polarizer used two high-power diode laser arrays. External-cavity line-narrowing technology was used to provide a narrow-spectrum and cost-effective light source. The full-width-half-maximum of the laser spectrum was narrowed from 2-3 nm to 0.2 nm. A new configuration of the laser-diode arrays involving orthogonal orientation was developed to increase the beam power and homogeneity. Two-axis beam-shaping optics was also developed to couple the light to the glass polarization chamber efficiently.

The polarizer system was built inside and around a 10120 gauss superconductcting magnet to reduce the gaseous and solid xenon relaxation and to provide a single homogeneous field for all aspects of the polarization process. Static spin-exchange optical pumping reached a high level of more than 87% polarization.

We investigated the magnetic field effect on the spin-exchange rate constant with real-time NMR measurements. Furthermore, the pumping chamber was placed at a position with lower magnetic field for control experiments. We found that even at our cell gas composition of xenon 37 torr, nitrogen 365 torr, and helium 3247 torr, the residual van der Waals spin-exchange interaction could not be ignored. The 10120 gauss field apparently quenched this helpful process.

Various uncoated or coated pumping cells were built and their wall relaxation time constants were measured to find a better coating method to increase xenon polarization. A SC-77 coating method showed better results than others.

The polarized xenon gas was applied to a xenon gas diffusion coefficient study and also to several rabbit lung MRI imaging studies. Highest thawed-out xenon polarization was 17.9 %.

The work described in this thesis provided data and findings helpful for the future design of advanced, cost-effective and easy maintenance xenon gas polarizer.

List of figures

List of tables

Abbreviations and symbols

AFP	adiabatic fast passage
amg.	amagat, ideal gas density at 0 ^{0}C and 1 ATM.
ATM	atmosphere
B	holding magnetic field
B_1	oscillating magnetic field of applied radiofrequency wave
CCD	charge coupled device
c_K	the coupling coefficient,
DMDCS	dimethyldichlorosilane
F	focal length of a lens
FFT	fast Fourier transformation
FID	free induction decay
FWHM	full-width-half-maximum
G_x	gradient applied along X axis
G_y	gradient applied along Y axis
I_α	magnetic dipole of nucleon α
K	Kelvin temperature unit
k_B	Boltzmann constant
k_x	spacial frequency in X axis.
k_y	spacial frequency in Y axis
MITI	Magnetic Imaging Technologies, Inc.
MRI	magnetic resonance imaging
MTCS	methoxytrimethylsilane

$m_j^{+1/2}$	electron spin magnetic quantum number, +1/2 up direction.
m(x,y)	sample magnetization moments at position (x,y)
M_{xy}	magnetic moment on X-Y plane
NMR	nuclear magnetic resonance
$N_{\alpha\beta}$	relative angular momentum between ^{129}Xe atom α and ^{129}Xe atom β.
OTS	octadecyltrichlorosilane
P	polarization
P_{Rb}	rubidium electron polarization
P_{Xe}	^{129}Xe polarization
[Rb]	rubidium number density
$r_{\alpha\beta.}$	inter-atom distance $r_{\alpha\beta.}$
$\vec{S}$	spin angular momentum
SNR	signal to noise ratio
S(t)	MRI signal tracings in time domain
T_{wall}	wall relaxation time constant
V_{dd}	nuclear dipole-dipole relaxation
$V_{p\text{-}p}$	peak-to-peak voltage
V_{sr}	spin-rotation relaxation
T_1	longitudinal spin-lattice relaxation time constant
T_2	horizontal spin-spin relaxation time constant
T_1^*	apparent longitudinal spin-lattice relaxation time constant
T_2^*	apparent horizontal spin-spin relaxation time constant
TE	time to echo

TR	repetition time
5S	principal quantum number is 5, and orbital quantum number is 0.
5P	principal quantum number is 5, and orbital quantum number is 1
$\hbar$	Planck constant
Δ	inter-gradient mixing time for diffusion process
Δt	pulse duration
α	flip angle
Γ_{Rb}	rubidium electron spin relaxation rate constant
Γ_{Xe}	xenon relaxation rate
γ	gyromagnetic ratio
γ'	combined spin-exchange rate with contributions from van der Waals interaction and binary collisions ($\langle \sigma v \rangle_{SE}$).
γ_{SE}	xenon-rubidium spin exchange rate
$\gamma_{opt}(r)$	rubidium electron light absorption constant
δ	gradient duration
$\vec{\mu}$	magnetic dipole moment
Ω	ohm
$<\sigma\upsilon>_{SE}$	velocity averaged binary spin-exchange cross section
ω	Larmor frequency
ω_f	flipping angular velocity

Chapter 1 Introduction

1.1 Motivation

Since laser polarized ^{129}Xe was applied to biomedical research in 1994 (Albert, et al. 1994), its applications in magnetic resonance imaging (MRI), MR spectroscopy and chemistry surface studies have been increasing rapidly (Chupp and Swanson 2001; Oros and Shah 2004).

Hyperpolarized noble gas imaging is especially well suited for gas-phase lung imaging since the proton density in the respiratory tract and space is very low. Among other applications, it has been successfully applied to imaging of the regional extent of chronic obstructive pulmonary disease (Salerno, et al. 2002; Mata, et al. 2006).

Since ^{3}He has a larger gyromagnetic ratio than ^{129}Xe (Weast 1970), ^{3}He imaging generally has a higher MR signal-to-noise ratio (SNR). However, ^{129}Xe exists in the normal atmosphere and can be fractioned out from the air. Its price is lower than ^{3}He. Also, xenon has a significantly smaller diffusion coefficient than helium. It also presumably suffers less from the limits that diffusion places on resolution. This may compensate at some level for the lower SNR. Furthermore, ^{129}Xe is soluble in blood and has a large chemical shift when dissolved in erythrocyte and plasma (Tseng, et al. 1997). The chemical shift also correlates with the partial pressure of blood oxygen (Wolber, et al. 2000). The biomedical application of ^{129}Xe could be huge.

Regarding production of polarized noble gas, spin-exchange optical pumping of ^{129}Xe is more complicated and harder than ^{3}He. Because of physics limits, xenon

polarization is usually lower than that of ^{3}He, and needs to be separated out from other buffer gases. Optically pumped xenon typically has polarization level from 5-20%, while ^{3}He can achieve more than 40%. Some groups have achieved more than 20% of ^{129}Xe polarization by using several high power diode lasers and relatively sophisticated or complicated set up (Zook, et al. 2002 and Ruset, et al. 2006).

A cost-effective, convenient and energy-efficient xenon gas polarizer would be of tremendous value for promoting xenon magnetic resonance imaging.

1.2 Specific aims

The specific aims of this thesis research are:

1. To investigate the potential advantages of using a line-narrowed diode laser for spin-exchange optical pumping of ^{129}Xe.

2. To investigate the optimal gas mixture, magnetic holding field, temperature, laser power and other parameters when producing polarized ^{129}Xe for MRI applications.

3. To build an innovative "2nd generation" xenon polarizer with increased xenon polarization, cost-effectiveness and ease of maintenance.

4. To apply the polarized xenon gas to MR imaging, and demonstrate the efficacy of the "2nd generation" design.

5. To provide findings and parameters for future advanced xenon polarizer designs.

1.3 Dissertation overview

Chapter 2 describes the theory and design concepts of the new xenon polarizer. A general system schematic is presented.

Chapter 3 NMR polarimetry was used to measure xenon gas polarization. The general set-up, phantom studies and experiments on NMR polarimetry are presented.

Chapter 4 describes the design and test results of laser line-narrowing methods including injection locking and the use of external cavities. Simulations and results of two-orthogonal two-axis diode lasers and beam shaping optics are also presented. Methods to verify the matching of diode laser spectra with rubidium absorption lines are shown at the end.

Chapter 5 details the study of spin-exchange kinetics and its response to magnetic fields. Methods of Pulse NMR measurements of spin-exchange rate constants and intrinsic wall relaxation times are presented. The magnetic field effect on spin-exchange rate constants and xenon polarizations are presented.

Chapter 6 presents modified designs of "pumping cells" that increase performance. Several glassware and pumping-cell coatings and subsequent measurements of wall relaxation times are described.

Chapter 7 presents experimental results from optimization studies aimed at increasing the xenon polarization. Applications of hyperpolarized xenon gas to MRI diffusion studies and gas-phase lung imaging are shown at the end.

Chapter 8 presents a summary of some of our more important experimental results as well as discussing the potential for future work.

Chapter 2 Theory and design considerations

In this chapter we examine the basic principles of spin-exchange optical pumping, and consider its implications for the design of a practical polarizer. We include consideration of the effect of magnetic field strength on both spin exchange and xenon spin relaxation. We show how consideration of the spin-exchange process dictates certain aspects of the design of the polarizer.

2.1 Overview of Spin-exchange optical pumping

(Walker and Happer 1997)

Spin-exchange optical pumping is a two step process in which 1) alkali-metal atoms are optically pumped, and 2) spin is transferred from the alkali-metal valence electrons to noble-gas nuclei through a hyperfine interaction. The resulting polarization defined as:

$$P = \frac{n_+ - n_-}{n_+ + n_-} \tag{2.1}$$

where n_+ is the spin lined-up with the holding magnetic field and n_- is the spin lined in reverse with the field, can be much higher than is the case if the polarization is due solely to a thermal Boltzmann distribution. In applications such as those described in this thesis, the difference can be on the order of 10^5.

2.1.1 Optical pumping of rubidium electron

The 794.76 nm circularly polarized laser light corresponds to the Rb D1 transition. The Rb ground state has $nL_J = 5S_{1/2}$, thus, the ground state has two sublevels with $m_j = \pm 1/2$. As light is absorbed, one of the two ground states is depopulated. If it were not for

electronic spin relaxation, the Rb polarization would rapidly approach 100%. Unfortunately, as the laser tends to push the Rb polarization higher, the electronic spin relaxation tends to push it lower.

The rubidium polarization can be described by the rate equation:

$$\frac{d\mathrm{P}_{Rb}}{dt} = (1-\mathrm{P}_{Rb})\gamma_{opt} - \mathrm{P}_{Rb}\Gamma_{Rb} \tag{2.2}$$

where Γ_{Rb} is the rubidium electron spin relaxation rate constant, and $\gamma_{opt}(r)$ is the optical pumping rate which can be obtained by:

$$\gamma_{opt}(r) = \int \Phi(r,v)\sigma(v)dv \tag{2.3}$$

where $\Phi(r,\upsilon)$ is the laser power-spectrum distribution, and $\sigma(\upsilon)$ is the photon absorption cross section. The rate equation can be solved to obtain the rubidium polarization equation in the time domain.

$$P_{Rb} = \frac{\gamma_{opt}}{\gamma_{opt}+\Gamma_{Rb}}[1-e^{-(\gamma_{opt}+\Gamma_{Rb})t}] \tag{2.4}$$

Unfortunately, for alkali-metal/xenon spin exchange, the major source of rubidium relaxation usually comes from xenon itself. High xenon gas density will reduce rubidium polarization and subsequently reduce xenon polarization.

2.1.2 Rubidium-xenon spin-exchange and xenon relaxation

Both binary collisions between rubidium and xenon and three-body collisions that result in van der Waals molecules can transfer angular momentum from the electron spin to the ^{129}Xe nucleus. The rate equation is:

$$\frac{d\mathrm{P}_{Xe}}{dt} = (\mathrm{P}_{Rb} - \mathrm{P}_{Xe})\gamma_{SE} - \mathrm{P}_{Xe}\Gamma_{Xe} \tag{2.5}$$

where γ_{SE} is the xenon-rubidium spin exchange rate and Γ_{Xe} is the xenon relaxation rate. This equation can be solved to obtain the xenon polarization equation in the time domain:

$$P_{Xe} = \left(\frac{\gamma_{SE}}{\gamma_{SE} + \Gamma_{Xe}} \right) P_{Rb}[1 - e^{-(\gamma_{SE} + \Gamma_{Xe})t}] \tag{2.6}$$

Thus, the xenon polarization is dependent on the rubidium polarization, the spin-exchange rate, and the xenon wall-relaxation rate. From this equation, it can be seen that the saturation polarization increases as $\Gamma_{Xe} \rightarrow 0$. Furthermore, as γ_{SE} gets bigger, the saturation polarization gets bigger, and the polarization at any time t gets bigger.

2.2 Spin-exchange kinetics

2.2.1 Introduction

Spin exchange between rubidium and xenon includes two kinds of collision interactions. One kind takes place when rubidium and xenon combine into a loosely bound van der Waals molecule during a three-body collision. Typically, xenon, nitrogen or helium could be the third body. Van der Waals molecules are suppressed at higher gas pressures (≥700 torr) and high magnetic field (≥200 Gauss) (Bhaska et al., 1983). Another kind of spin exchange interaction is binary collisions between rubidium and xenon which have a very short lifetime of ~10^{-12} seconds and are relatively independent of gas pressure and magnetic field.

As discussed by Cates et al, 1992, the longitudinal apparent spin relaxation rate $1/T_1^*$ of ^{129}Xe in a moderate pressure glass cell is:

$$\frac{1}{T_1^*} = [Rb]\left(\frac{\gamma_M \zeta}{[Xe]} + \langle \sigma v \rangle_{SE}\right) + \Gamma_{Xe} \qquad (2.7)$$

where [Rb] is the rubidium number density, γ_M is a constant, ζ is nearly constant and depends on the nuclear spin relative abundance of each isotope in rubidium, and $<\sigma\upsilon>_{SE}$ is the velocity averaged binary spin-exchange cross section. Also, Γ_{Xe} is the xenon relaxation rate due to wall collisions and magnetic field inhomogeneity.

For xenon pressure greater than roughly 350 torr, the spin-exchange rate due to binary collisions exceeds the spin-exchange rate from the formation of van der Waals molecules even at low magnetic field. Relaxation due to van der Waals molecules is inversely proportional to the third-body pressure, while relaxation due to binary collisions is pressure independent. Equation 2.6 can be simplified as:

$$\frac{1}{T_1^*} = [Rb]\gamma' + \Gamma_{Xe} \qquad (2.8)$$

where γ' includes contribution from van der Waals molecules and binary collisions ($\langle \sigma v \rangle_{SE}$).

Note that according to equation 2.8, a series of measurements of $1/T_1^*$ as a function of [Rb] can be used to determine γ' and Γ_{Xe}.

2.2.2 Theoretical consideration of spin-exchange rate constant and magnetic field

Bouchiat et al. (1972) found that in a glass cell filled with rubidium and noble gas, the relaxation rate of polarized rubidium was magnetic-field dependent. From the decoupling magnetic-field width of 10 Gauss, they suggested the existence of some characteristic interaction time on the order of 10^{-8} seconds, whereas normal collision duration in the gas phase was typically 10^{-12} seconds. Further investigation revealed that there were three

types of relaxation mechanism for the polarized rubidium vapor: 1) van der Waals molecules, 2) binary collisions, and 3) wall relaxation. Of these, relaxation taking place in van der Waals molecules was magnetic field dependent, while relaxation taking place in binary collisions was magnetic field independent.

The magnetic-field dependence was attributed to a phenomenon in which the precession period of the Rb electronic spin due to the externally applied magnetic field becomes comparable to *the lifetime of the van der Waals molecule*. As the gyromagnetic ratio ($\gamma/2\pi$) of electron is 2.80 x 10^4 MHz/Tesla (Weast 1970), in a magnetic field of 10 gauss, the Larmor frequency will be 28 MHz (equation 2.9):

$$\omega = \gamma B \tag{2.9}$$

where ω is the Larmor frequency in radian per second, γ is the gyromagnetic ratio, and B is the holding magnetic field. The equivalent precession period is 3.6 x 10^{-8} seconds, which is on the order of van der Waals process's lifetime. Since the van der Waals molecular lifetime is longer than the precession period, the spin-exchange contribution from the molecules will be reduced. Similarly, since binary collisions have a lifetime of ~10^{-12} seconds, more than 20 Tesla field would be needed to decouple the spin exchange.

2.2.3 Review of published spin-exchange kinetics studies

Spin-exchange rates at different gas compositions, pressures, and magnetic fields have been reported in the literature.

In keeping with one might expect from the work of Bouchiat et al. (1972), Bhaskar et al. (1983) found the longitudinal relaxation of ^{129}Xe nuclear spins slowed down substantially in an external magnetic field of about 100 Gauss. At nitrogen pressure of 9.7 torr, xenon 0.5 torr and a few gauss field, they measured a combined spin-

exchange rate γ' to be ~2.5 x 10^{-14} cm^3s^{-1}. They showed that binary collisions contribute no more than a few percent to the spin-exchange rate at very low gas pressure and magnetic field. They also found that with higher buffer-gas pressure, higher magnetic fields were needed to slow down the spin-exchange rate. The 50% magnetic decoupling field vs. nitrogen buffer gas pressure had a slope of 1.6 gauss/torr.

Cates et al. (1992) measured three-body and binary collisions rate at hundreds torr pressure and 0.11 gauss. They found that $\langle \sigma v \rangle_{SE}$ was 3.7 x 10^{-16} cm^3s^{-1} and that the contribution to spin-exchange from van der Waals molecules decreased as the buffer gas pressure increased. There was still a little van der Waals activity of 1.2 x 10^{-16} cm^3s^{-1} at a high xenon pressure of 1817 torr. In this study, they used the Killian formula to deduce the rubidium density (Killian, T. 1926).

Rice and Raftery (2002) measured rubidium-xenon spin-exchange and relaxation rates at high pressures and high field (47000 gauss). Surprisingly, they still measured a van der Waals rate constant of 1.4 x 10^{-16} cm^3s^{-1} (303 torr, buffer gas), and 0.26 x 10^{-16} cm^3s^{-1} (1654 torr, buffer gas). They measured $\langle \sigma v \rangle_{SE}$ to be 0.6 x 10^{-16} cm^3s^{-1}, which was significantly smaller than that measured by Cates et al. in 1992. They observed a decreased van der Waals rate constant and cell-wall relaxation rate as the buffer gas pressure increased. In this study they also used the Killian formula (Killian, T. 1926).

Jau et al. (2002) measured ^{129}Xe-Rb spin-exchange rate to be 1.75 +/- 0.12 x 10^{-16} cm^3s^{-1}. The experiment was intentionally conducted under ~600 torr and 94000 gauss condition to minimize the van der Waals contribution as much as possible. They used the Faraday rotation method to measure the rubidium density directly (Wu et al. 1986).

The literature consistently shows a trend in which the van der Waals process is decreased with high gas pressure and high magnetic field. There is some inconsistency, however, regarding the details. For example, Rice and Raftery (2002) reported residual van der Waals activity at 47000 Gauss, and an anomalously small binary spin-exchange rate.

The value of the combined spin-exchange rate γ' has not previously been determined for our operating cell conditions of xenon 37-71 torr, N_2 365 torr, and ^{4}He 3210-3247 torr. We thus found it valuable to measure γ' directly to better understand this less-explored region of spin-exchange parameters, as well as to better understand our apparatus.

2.3 ^{129}Xe spin relaxation and magnetic field

Laser polarized xenon gas is accumulated in a separate liquid nitrogen cold bath to separate xenon from other buffer gases. At the end, the xenon ice is thawed-out. With the accumulation time approaching from 30 minutes to 90 minutes, the relaxation rate of solid xenon plays an important role in determining the final polarization.

High magnetic field and xenon relaxation

Kuzma et al. (2002) pointed out that even though the xenon accumulator was immersed in a liquid nitrogen bath (77 K) apparently, however, as xenon ice accumulated inside of the glass wall, the temperature of piled-up xenon gradually increased to ~145 K (melting point of xenon) at the top surface, where newest frozen-out xenon deposited. There was a temperature gradient. Therefore, the solid ^{129}Xe relaxation time constant in the accumulator was not a single value, but an integral of different T_1 from hours to

seconds. They studied the solid xenon relaxation rate at different temperatures and magnetic fields and found that the nuclear dipole-dipole relaxation process V_{dd}:

$$V_{dd} = \frac{\mu_\alpha \mu_\beta}{\mathrm{I}_\alpha \mathrm{I}_\beta r^3{}_{\alpha\beta}} \left[\mathrm{I}_\alpha \cdot \mathrm{I}_\beta - 3 \frac{(\mathrm{I}_\alpha \cdot r_{\alpha\beta})(r_{\alpha\beta} \cdot \mathrm{I}_\beta)}{r^2{}_{\alpha\beta}} \right] \qquad (2.11)$$

(where I_α is the nuclear spin of ^{129}Xe atom α, I_β is the nuclear spin of ^{129}Xe atom β, and $r_{\alpha\beta}$ is the inter-atom distance), was the major relaxation mechanism for solid xenon at temperature above 120 K, and the relaxation time constant T_1 could be as short as 6 seconds. Interestingly, the nuclear dipole-dipole relaxation mechanism was magnetic field dependent. The solid xenon relaxation rate, at temperature above 120 K, could drop two orders of magnitude from a field of 670 gauss to 14300 gauss.

The other major ^{129}Xe spin relaxation (V_{sr}) in gaseous, and solid xenon at temperature between 50 K and 120 K is caused by the spin-rotation mechanism V_{sr}:

$$V_{sr} = c_K(r_{\alpha\beta})\mathrm{I}_\alpha \cdot \mathrm{N}_{\alpha\beta} \qquad (2.10)$$

where c_K is the coupling coefficient, I_α is the nuclear spin of ^{129}Xe atom α, $r_{\alpha\beta}$ is the inter-atom distance, and $\mathrm{N}_{\alpha\beta}$ is the relative angular momentum between ^{129}Xe atom α and ^{129}Xe atom β. The relaxation time constant is on the order of hours below 120 K (Cates et al. 1990, Kuzma et al. 2002).

Field homogeneity:

Gamblin and Carver (1965) showed that inhomogeneous magnetic fields could increase the transverse and longitudinal spin relaxation. The longitudinal spin-relaxation due to magnetic field gradient is given by:

$$\frac{1}{T_1} = D\frac{\left|\vec{\nabla} B_x\right|^2 + \left|\vec{\nabla} B_y\right|^2}{B_z^2} \qquad (2.12)$$

where T_1 is the longitudinal spin relaxation time constant, D is the gas diffusion coefficient, $\vec{\nabla} B_x$ is the spatial gradient of magnetic field along X axis, and B_z is the holding magnetic field (Cates, et al. 1988).

The findings that high and homogeneous magnetic field can decrease spin relaxation were important for the design of a new xenon gas polarizer.

Judging from the theories presented in section 2.2 and 2.3, we speculate that operating xenon polarizer at high magnetic field has both advantage and disadvantage factors. We will investigate this problem in Chapter 5.

2.4 NMR preliminary

(Nishimura 1996)

The laser-polarized ^{129}Xe will need a quantitative measurement to determine its polarization. We present the basic principle of NMR as a preparation for NMR polarimetry.

In analogy to the precession of a spinning top under a gravitational field, a spinning magnetic moment in an external magnetic field will also precess. Some nuclei such as ^{1}H, ^{3}He and ^{129}Xe belong to spin-1/2 species, while ^{4}He is spin-0. For a nuclear magnetic moment μ with intrinsic spin angular momentum S, the torque equation under external magnetic field B can be expressed as:

$$\frac{d\vec{S}}{dt} = \vec{\mu} \times \vec{B} \qquad (2.13)$$

Using the definition of the gyromagnetic ratio γ:

$$\vec{\mu} = \gamma\vec{S} \tag{2.14}$$

and inserting Equation 2.14 into Equation 2.13, we obtain the Larmor equation:

$$\omega = \gamma B \tag{2.15}$$

where ω is the precession frequency of the nuclear magnetic moment. It is determined by the moment's gyromagnetic ratio γ and the external field B. The $\gamma/2\pi$ of ^{1}H is 42.576 MHz/Tesla, while that of ^{129}Xe is 11.777 MHz/Tesla (Weast, 1970).

Generalizing Equation 2.13 and 2.14 to a group of magnetic moments with net moment M (Mx, My, Mz) under external magnetic field B, incorporating the empirical longitudinal relaxation time constant T_1 and transverse relaxation time constant T_2, we are at the Bloch equations:

$$\frac{dM_x}{dt} = \gamma(M \times B)_x - \frac{M_x}{T_2} \tag{2.16}$$

$$\frac{dM_y}{dt} = \gamma(M \times B)_y - \frac{M_y}{T_2} \tag{2.17}$$

$$\frac{dM_z}{dt} = \frac{M_0 - M_z}{T_1} + \gamma(M \times B)_z \tag{2.18}$$

An external oscillating magnetic field B_1 at Larmor frequency ω, can flip the magnetic moments:

$$\omega_f = \gamma B_1 \tag{2.19}$$

where ω_f is the flipping angular velocity. The flip angle α after a pulse duration of Δt equals:

$$\alpha = \omega_f(\Delta t) \tag{2.20}$$

With B along the Z axis, B_1 along either X or Y axis, following an α degree pulse, the original magnetic moment M_0's projection on the X-Y plane, M_{xy}, has a time evolution which can be expressed as:

$$M_{xy}(t) = M_0 \sin(\alpha) e^{-\frac{t}{T_2}} \tag{2.21}$$

The longitudinal component M_z has a time evolution of:

$$M_z(t) = M_0 + (M_0 \cos(\alpha) - M_0)\left(1 - e^{-\frac{t}{T_1}}\right) \tag{2.22}$$

2.5 Design considerations and general schematic of new xenon gas polarizer

(Fig. 2.1)

The polarizer is based on the technique of spin-exchange optical pumping. Since xenon is very depolarizing to rubidium spins, dilute xenon gas is used in the pumping chamber. Laser polarized xenon gas is accumulated in a separate liquid nitrogen cold bath. At the end, the xenon ice is thawed-out and applied for animal or human lung imaging.

We applied theory and findings that were discussed in sections 2.1 to 2.3 to the design considerations. Additional principles include simplicity, cost effectiveness, and easiness for maintenance.

Superconducting magnet:

As described in section 2.3, solid ^{129}Xe relaxation rate decreased in high and homogeneous magnetic. Both improvements can increase xenon polarization. To reduce

the xenon relaxation in pumping cells, transfer tubing and accumulator, we decided to put all of them inside the bore of a superconducting magnet.

This magnet was made by Oxford Instruments. The bore dimension was 152 cm in length and 40 cm in diameter. The center magnetic field was ramped up to 10120 gauss. The magnetic field profile will be presented in section 3.3. This magnet served as the holding field for both spin-exchange optical pumping and the nuclear magnetic resonance measurement.

Optical system:

Laser source is essential to a noble gas polarizer. We noticed that the newly developed external-cavity line-narrowing technology for diode laser had not yet been incorporated into a full, well developed, practical scheme for routinely polarizing xenon. It is more energy-efficient and cost-effective than using un-narrowed high power fiber-coupled diode laser arrays (Chann, et al. 2000). Therefore, we decided to incorporate this technology into our system. Even though line-narrowing technology can reduce the laser spectrum width down to ~0.2 nm, this is still approximately equal to the pressure-broadened rubidium absorption width. To increase the light absorption, we would still need pressure broadening in our cell. (Pressure broadening is the phenomenon in which rubidium has a wider absorption line width with increased buffer-gas pressure.) Our pumping cell was operated at a pressure near ~4560 torr when heated up to near 100 ^{0}C for pressure broadening. Higher pressure runs a risk of explosion.

The optical table for line-narrowing set-up was placed near the superconducting magnet. Line-narrowed laser light was reflected by a mirror to enter the magnet bore and was coupled to the pumping cell window. For stable collimation and coupling of laser

light to the pumping cell inside of the bore, the optical table and the magnet were connected by several custom-built aluminum rods and plates to fix their relative position. The details of optics and line-narrowing set-up will be described in Chapter 4.

NMR system:

To investigate the spin-exchange kinetics and optimize the xenon gas polarizer, a real-time measurement of ^{129}Xe polarization was needed. We designed a Helmholtz configuration pick-up coil to enclose the pumping cell in order to study polarization during closed cell optical pumping and actual flowing condition that were used when accumulating xenon. Both the coil and the glass cell were inside the heating oven. It turned out to be invaluable that we could perform nuclear magnetic resonance measurement throughout the spin-exchange optical pumping cycles. To improve the signal-to-noise ratio, the preamplifier of the nuclear magnetic resonance system was placed near the Helmholtz coil inside of the magnet. Tests were performed to ensure that it was functioning well at 10000 gauss field.

In addition to the pick-up on the pumping cell, we also had a separate probe that operated within the same magnet that was specifically designed to accommodate a small sampling bulb. The compact nature of this other system permitted us to calibrate it with significantly higher accuracy. It was used exclusively to measure the thawed-out xenon gas polarization. Both the Helmholtz coil and the solenoid were operated at the same Larmor frequency. This simplified the system. The main electronics and instruments were located 2 meters away from the magnet. The details of the NMR system will be presented in Chapter 3.

Gas Handling system:

The Helmholtz coil, pumping cell, and oven were located at the center of the bore. Heated air entered the oven to heat up the pumping chamber. A new vacuum and gas handling system was built for this new xenon polarizer. The layout was similar to the original continuous flow polarizer as described by Driheuys, et al.(1996). The gas handling system was located ~1 meter away from the magnet. It supplied xenon mixture gas to the pumping cell. Gas exiting from the cell was transferred to an accumulator which was 4 inches posterior to the oven. A liquid nitrogen Dewar enclosed the accumulator to freeze out xenon during continuous flow operation. Exhaust buffer gas was transferred back to the gas panel. When accumulated xenon had reached certain amount, it was thawed out and expanded into a small sampling bulb and a plastic bag connected to the accumulator. The sampling bulb was then put into a small NMR probe for xenon polarization measurement. The bag of gas was sent to a nearby room for magnetic resonance imaging studies.

Pumping cell, coatings and tubing:

The pumping cells were similar to those used in the commercial MITI xenon polarizer, except that we added some modifications to increase its efficacy. The pumping cell could still be easily refurbished and maintained. The tubing was flexibly connected and could be taken out for replacement conveniently. Improvements on cell designs and coatings will be presented in Chapter 6.

Non-magnetic components:

Since the whole system was built inside and around a superconducting magnet, all the materials and components were non-magnetic.

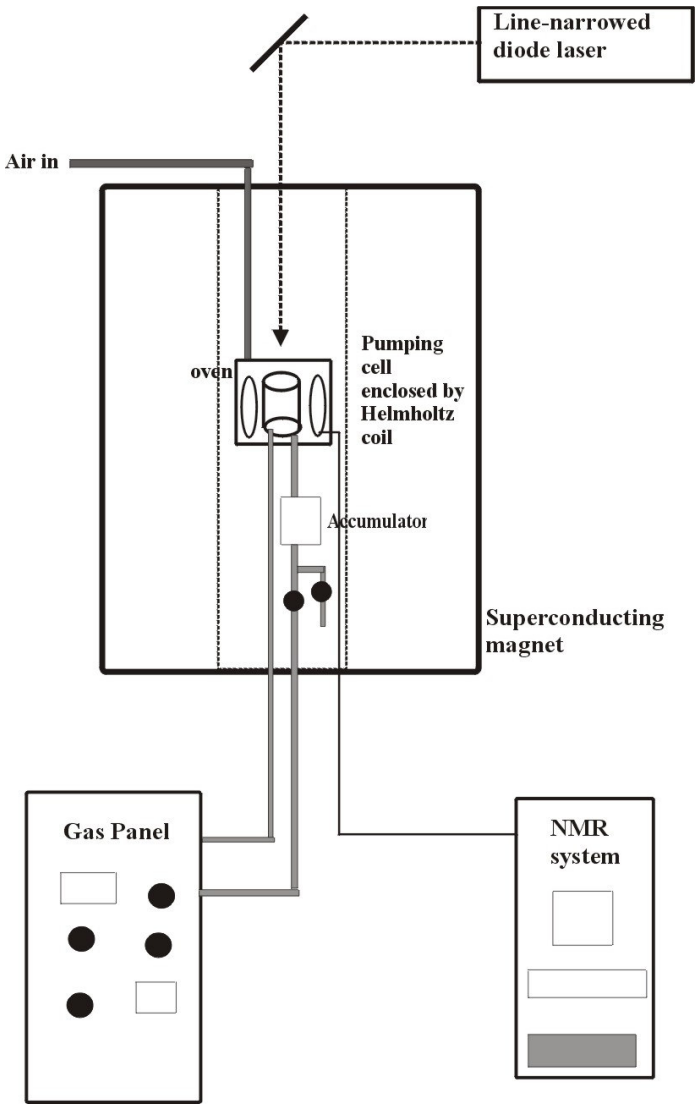

Fig. 2.1 General schematics of new xenon gas polarizer

The superconducting magnet was ramped up to 10120 gauss. It served as the holding field for both spin-exchange optical pumping and NMR measurement. The oven, pumping cell, accumulator and some connecting tubes were inside of the magnet bore. A Helmholtz coil enclosed the pumping cell for real-time NMR measurement. Both coil and glass cell were inside of the oven which was located at the center of the magnet bore. The external-cavity line-narrowed laser light was reflected by a mirror to enter the bore and coupled to the pumping cell window. A gas and vacuum system was located ~1 meter away from the magnet. It supplied xenon mixture gas to the glass cell. Exit gas from the cell flew through the accumulator. The accumulator was immersed in a liquid nitrogen bath to freeze out xenon from other buffer gases. Useless buffer gases were transferred back to the panel to be exhausted to the atmosphere. When accumulated xenon reached certain amount, it was thawed-out by a warm water bath and expanded into a bag and a sampling glass bulb. The sampling bulb was then put into a small NMR probe inside of the magnet for polarization measurement. A NMR electronics rack was located ~2 meters away from the magnet. The bag of gas was finally sent to a nearby room for magnetic resonance imaging study.

Chapter 3 Nuclear magnetic resonance apparatus and polarimetry

3.1 Introduction

The polarization level of the xenon gas needed to be quantitatively measured. Both continuous adiabatic free passage (AFP) and pulse NMR can be used for this purpose. In AFP, the holding field is swept slowly while the RF frequency is held constant. The disadvantage of AFP is its relatively long duration. While it is useful in ^{3}He measurements, it is less convenient for a fast depolarization species like ^{129}Xe. We chose pulse NMR to do ^{129}Xe polarimetry because it is faster. For calibration we used both samples of water and xenon whose polarizations were at thermal equilibrium.

3.2 Thermal equilibrium polarization

(Rolf 1994)

The potential energy of a magnetic moment in an external field B is:

$$E = -\mu \cdot B \tag{3.1}$$

From quantum mechanics, the nucleon's intrinsic spin angular momentum S is quantized in z direction to $Sz = \pm 1/2\,\hbar$. The energy difference between the spin-up (n_+) and spin-down (n_-) state nucleons is:

$$\Delta E = \gamma \hbar B \tag{3.2}$$

From the Boltzmann distribution:

$$\frac{n_-}{n_+} = e^{-\frac{\Delta E}{k_B T}} \tag{3.3}$$

where k_B is Boltzmann's constant, and T is the absolute temperature in Kelvin.

By definition, polarization **P** equals:

$$\mathrm{P} = \frac{n_+ - n_-}{n_+ + n_-} \cong \frac{\Delta E}{2k_B T} = \frac{\gamma \hbar B}{2k_B T} \tag{3.4}$$

Our superconducting magnet was ramped up to 10120 gauss, which resulted in a ^{129}Xe Larmor frequency of 11.921 MHz. To calibrate the xenon probe, we measured the ^{1}H and ^{129}Xe signal with the same probe and at the same frequency. The proton's and the ^{129}Xe's thermal equilibrium polarization at this frequency are both 9.77 x 10^{-7} at room temperature (20 ^{0}C). We used this value often in our calibrations as discussed in section 3.4.

3.3 pulse NMR apparatus

(Fukushima and Roeder 1981)

Two pulse NMR apparatus were custom built for measuring xenon polarizations. The major components included magnets, electronics system, probes and Labview programs.

3.3.1 Magnet:

A good magnet should provide a homogeneous and stable holding field for NMR measurement. Inhomogeneous fields will dephase the flipped spins, shorten the T_2^* time constant and thus reduce signal strength. The field should also be stable enough such that the radio pulse will be resonant in a reproducible way.

Electromagnet:

An electromagnet was used for our NMR experiments in our main laboratory in Physics. It was after some initial struggles that we realized this magnet needed additional shim coil to make its field more homogeneous. A pair of Maxwell shimming coils was built by our colleague Scott Rohrbaugh. This magnet performed especially well near 2000-6000 gauss. We used it to do NMR polarimetry and xenon relaxation time constant measurements.

Superconducting magnet:

We were able to obtain a retired Oxford magnet. We could energize this magnet to a custom field within its 47000 gauss range. To avoid large fringe field, it was only energized to 10120 gauss. This magnet provided holding field for both spin exchange optical pumping and pulse NMR measurement.

Shown in Fig. 3.1 is a typical superconducting coil circuit. Initially, the whole coil is superconducting under liquid helium bath. For energizing or de-energizing, we run current through a small resistor nearby the main superconducting coil. A small segment of the main coil is slightly heated and loses its superconducting status. The main coil circuit can then conduct with the outside circuit loop where we apply voltage to energize or de-energize to a desirable level. Afterwards, we turn off the heating resistor and the coil is again fully superconducting. The main current will then circulate by itself indefinitely, so long as we refill the liquid helium and nitrogen periodically. There are additional small superconducting shimming coils built inside the magnet that are controlled similarly.

A complete field mapping was done for the magnet. The most homogeneous spot was reserved for a Helmholtz coil that enclosed the pumping cell for real-time pulse

NMR polarization measurements. The Helmholtz coil and the cell were both inside an oven. Another small solenoid coil for thawed-out xenon measurement sat in front of the oven. The solenoid coil was later moved to the "sweetest spot" when we moved the oven outside of the magnet for a different consideration that will be explained in later chapters. An accumulator for freezing out xenon sat behind the oven (Fig. 3.2).

3.3.2 General schematic of NMR apparatus

A personal computer controlled the system by sending out a trigger pulse to a pulse generator. The pulse generator then sent out a specific pulse to a function generator to emit a RF sinusoidal wave. The RF sine wave was amplified by a power amplifier. Two crossed diodes reduced the noise input to the probe when the power amplifier was silent. The probe coil was driven by the amplified RF wave. Generated NMR signals were then collected by a ¼ wave line to be amplified by a preamplifier. The ¼ wave line served to protect the sensitive preamplifier during power amplifier firing. Output signals from the preamplifier went through a mixer to be mixed down to audio-frequency sine waves, and then further amplified by a second stage amplifier. A digital oscilloscope digitized and recorded the NMR signal. The personal computer acquired the final signal and stored it. (Fig. 3.3)

3.3.3 Probe

As shown in Fig. 3.4, the coil inductor and tuning capacitor formed a serial tank resonator. The resonant frequency was tuned to the Larmor frequency. A parallel matching capacitor matched the impedance of the probe circuit to 50 Ω.

Both a Helmhlotz coil and a solenoid coil were used in the system. The Helmholtz coil enclosed the pumping cell for real time polarization monitoring. The solenoid coil

could accommodate a small gas sampling bulb of ~2 cm diameter which was used to measure the polarization of thawed-out xenon when running the polarizer.

3.3.4 Labview control and data acquisition program:

Some Labview programs were written for control and data acquisition of the NMR experiment. Several additional programs were written to do signal averaging, Fourier transformation, noise reduction, and data fitting (Fig. 3.5).

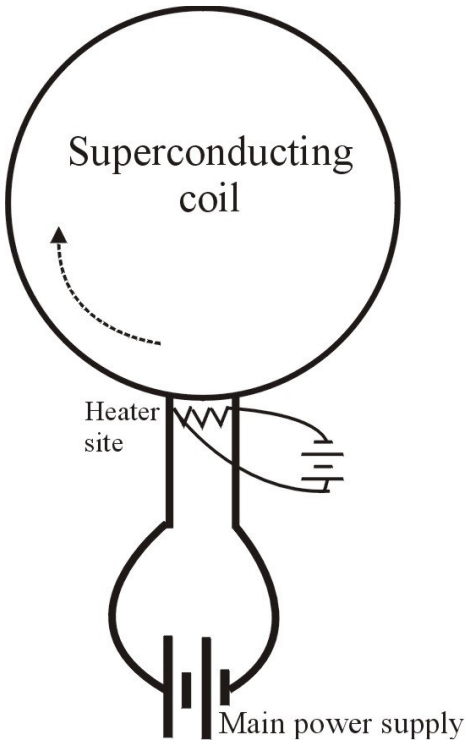

Fig. 3.1 superconducting coil circuit. The whole coil is immersed in liquid helium to maintain its superconducting status. A small resistor is located near the superconducting coil. When the resistor is heated up, the near-by segment of the main coil loses its superconducting status. The main coil sees that the outside circuit loop has lower resistance and could form a closed circuit with the outside loop. A main power supply connected to the outside loop can therefore energize the superconducting coil. When the main current is adjusted to a desired level, the small heater is turned off. That segment of main coil recovers its superconducting status. The main current will then circulate indefinitely.

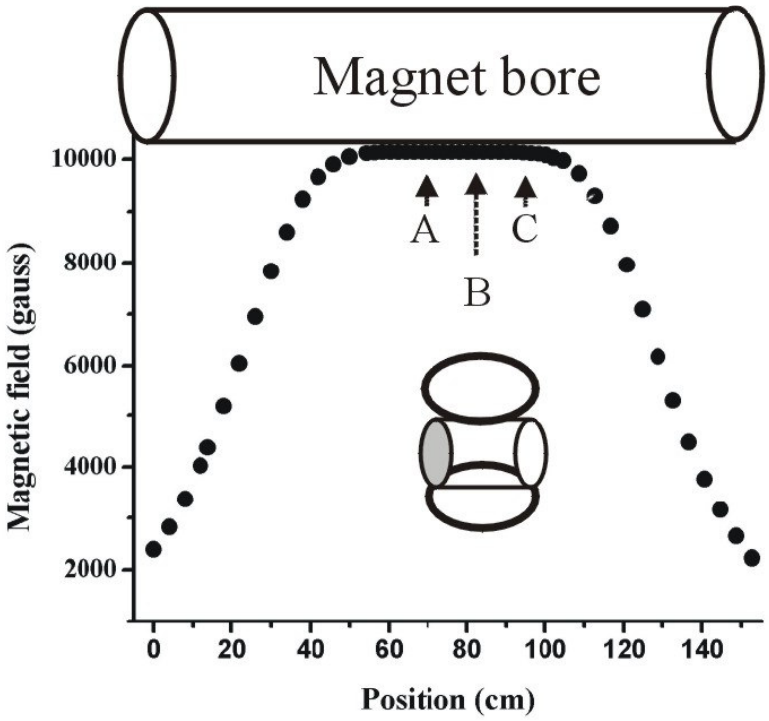

Fig. 3.2 Field mapping of the magnet and location of major components. The magnet bore span 152 cm with a diameter of 40 cm. The most homogeneous spot of position B (84 cm) was reserved for a Helmhlotz coil that enclosed the pumping cell for real-time pulse NMR polarization measurement. The Helmholtz coil and the cell were both inside an oven. Another small solenoid coil for thawed-out xenon measurement sat in front of the oven at position A. The solenoid coil was later moved to the sweetest spot when we moved the oven outside of the magnet for other consideration. An accumulator for freezing out xenon sat behind the oven at position C.

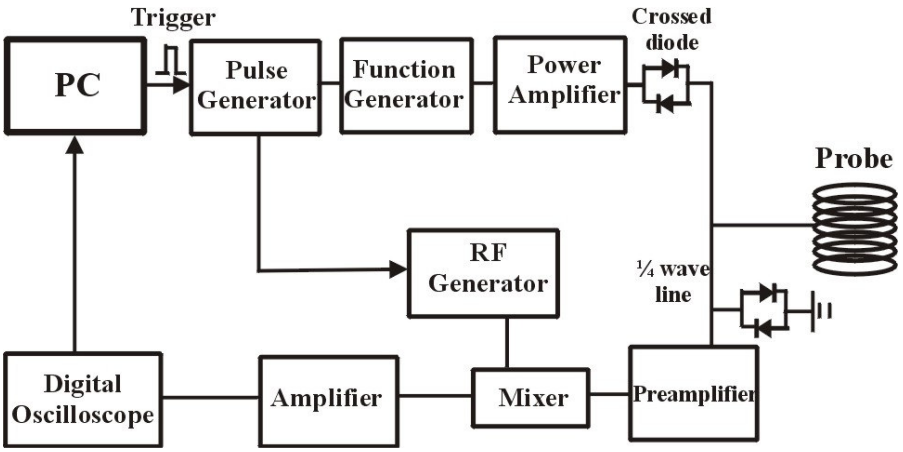

Fig. 3.3 Pulse NMR apparatus. A personal computer controlled the system by sending out a trigger pulse to a pulse generator. The pulse generator then sent out a specific pulse to a function generator to emit RF sinusoidal wave. The RF sine wave was amplified by a power amplifier. Two crossed diodes reduced the noise input to probe when power amplifier was silent. The probe coil was driven by the amplified RF wave. Generated NMR signal was then collected by a ¼ wave line to be amplified by a preamplifier. The ¼ wave line served to protect the sensitive preamplifier during RF power amplifier pulsing. Output signal from preamplifier go through mixer to be mixed down to audio-frequency sine wave, and then further amplified by a second stage amplifier. A digital oscilloscope digitized and recorded the NMR signal. The personal computer acquired the final signal and stored it.

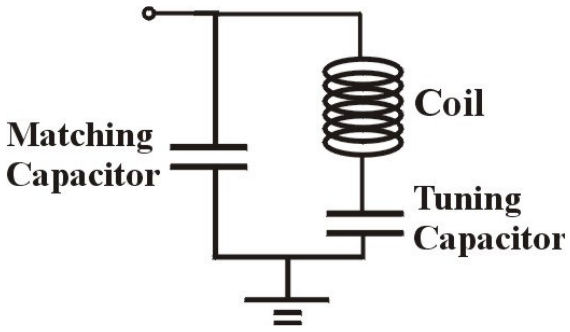

Fig. 3.4 NMR probe circuit. The coil inductor and tuning capacitor form a serial tank resonator. They resonate near the Larmor frequency. A parallel connected matching capacitor match the impedance of the probe circuit to 50 Ω, which is a common value of RF circuit.

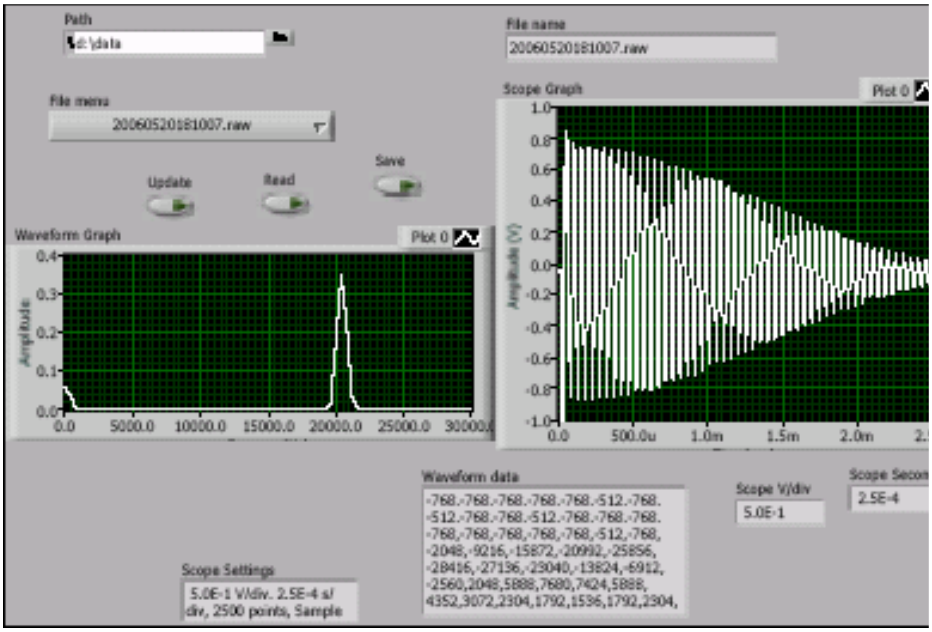

Fig. 3.5 Sample of Labview program. This Labview program could read in experimental data, do FFT analysis and write out the data in matrix format. The right side tracing was a free induction decay tracings of thawed-out xenon of 17.9% polarization. The left side was its Fourier transformation amplitude.

3.4 water and xenon phantom calibration

The NMR polarimetry needs a standard to do the calibration. To be accurate as much as possible, we used both water (^{1}H) and xenon (^{129}Xe) phantom for calibration. The water signals were obtained in the electromagnet because we can adjust its magnetic field easily, while the xenon signals were measured in the superconducting magnet. Because of small uncertainties in pressure measurement when preparing the xenon phantom cell, the water signals were used to cross-calibrate the pressure of the xenon phantom cell. The calibrated xenon phantom signals were then used to calibrate the polarization of thawed-out xenon gas. The details will be presented in section 3.4.1 to 3.4.4.

We also prepared a xenon phantom cell of the same dimension as the cylindrical

pumping cell which was enclosed by a Helmholtz coil for real-time NMR measurements. The NMR measurement was done in the superconducting magnet. The details of this calibration will be presented in section 3.4.5.

3.4.1 Dimension and volume of phantom cells

Dimension of 2 cm water cell:

The water cell diameter was 1.99 cm. Its wall thickness was ~0.06 cm. Water filled the ball only, and did not extend up to the stem. Calculated volume was 3.424 cm^3.

Dimension of 2 cm xenon cell:

Xenon cell diameter was 1.98cm. Its wall thickness was ~0.06 cm. The stem length was 0.9 cm and stem inner diameter was ~0.43cm. Calculated ball volume was ~ 3.369 cm^3 and the stem volume was ~0.13 cm^3. Since stem volume was less prone to RF pulse, we weighed it as 50%, and counted it as ~0.065 cm^3. Therefore, total effective xenon cell volume was ~3.434 cm^3. The volume ratio of xenon/water equaled 1.003.

3.4.2 Water sphere cell free induction decay experiment in the electromagnet.

To provide a cross calibration for the xenon phantom cell, we measured ^1H signal at 11.921 MHz (the same Larmor frequency used in the superconducting magnet), in the electromagnet (experiment time and file name: 20060719153002, 20060719153137, 20060719153235).

A small solenoid probe that can accommodate a 2 cm sphere was used in this study. For free induction decay measurement, 90-degree pulse was used. Either pulse strength or duration was varied repeatedly and sequentially to find the 90 degree, 180 degree and 360 degree pulse. Either single shot or longer pulse interval was compared to

our chosen pulse interval when doing averaging data acquisition to avoid T_1 recovery problems. For the water signal, the function generator was set at a frequency of 11.921 MHz, an amplitude of 1.0 volts, a pulse duration of 40 μsec, and was pulsed with an interval of more than 50 seconds. The computer was used to accumulate and average 3 single shot signals. Total system amplification used was 17600 fold from the probe to the oscilloscope.

Shown in Fig. 3.6 is the free induction decay curve of water signals using a small solenoid coil. The initial distortions were due to coil ringing.

In Fig. 3.7, the first ~50 μsec and tail noisy signals were truncated. Both upper and lower peak points were selected and registered. Small ripples less than 0.2 – 0.3 volts were discarded. The peaks were then fit with the equation: y = amplitude x $\exp(-x/T_2^*)$. The fits of both the upper peaks and lower peaks were plotted in Fig. 3.7. Fitting results are also listed in Table 3.1.

Table 3.1 Fitting results of water signal.

	Amplitude (volt)	T_2^* (sec)	R^2	Chi^2
upper peaks	3.266	480 μ	0.993	0.00325
lower peaks	3.249	480 μ	0.988	0.00661

Total water signal amplitude equaled 6.515 Volts. The normalized water signal amplitude was 3.702×10^{-4} Volts which equaled total signal amplitude divided by the system amplification.

3.4.3 Xenon sphere phantom cell experiment in the superconducting magnet.

The small solenoid coil was initially placed at position A (~70) cm position of the superconducting magnet. It was moved to position B (~84cm), the most homogeneous

part, later on (Fig. 3.2). The reasons of moving will be described in Chapter 5. NMR measurements at both sites are presented in this section.

Xenon phantom at ~84 cm location of the10120 gauss superconducting magnet

(experiment time and file name: 20060813162105)

For this procedure we used the same small solenoid probe as was used in the water phantom measurement. The 2 cm diameter small cell contained enriched ^{129}xenon (86.2%), 5:1 xenon/oxygen ratio at a pressure that was nominally measured to be 15 atmosphere pressure. The function generator was set to a frequency of 11.921 MHz, an amplitude of 950 mV, a pulse duration of 26.2 μsec and was pulsed every 20 seconds. The computer was used to accumulate and average 256 signals. Total system amplification equaled 257500 fold from the probe to the oscilloscope.

As shown in Fig. 3.8, the xenon signal had an apparent T_2^* much longer than water's ~0.5 msec. The signal decay was assumed to be negligible within 1 msec. The signal level around ~600 usec to 1 msec was measured to be 0.15 Volt. The normalized xenon signal was calculated to be 5.83E-7 Volt. Regular thawed-out xenon signal strength measured at the same position would be compared at the same ~600 μsec region.

Xenon phantom at ~70 cm position of the 10120 gauss superconducting magnet

(experiment time and file name: 20060518130030)

When the oven and pumping cell were located at the ~84 cm position, the small solenoid probe had to be put at the ~70 cm position, which was a less homogeneous spot. The same enriched xenon phantom cell was used in this measurement. The function generator was set to a frequency of 11.921 MHz, an amplitude of 500 mV, a pulse duration of 43 μsec, and was pulsed every 10 seconds. The computer was used to accumulate and

average 64 signals. Total system amplification equaled 515000 fold from the probe to the oscilloscope.

As shown in Fig. 3.9, the ~70 cm position was not as homogeneous as the ~84 cm position, and the T_2^* was shorter than at the ~84 cm. The measured signal strength at ~600 μsec was 0.23 Volts. Normalized xenon signal was calculated to be 4.47E-7 volt. Regular thawed-out xenon signals measured at ~70 cm position would use this calibration for polarimetry. The voltage near ~600 μsec region would be measured for calculation.

3.4.4 Cross calibration of xenon phantom cell pressure by water signal

The small enriched ^{129}Xe (86.2%) phantom cell with gas composition of Xe/O_2 5:1 ratio at a pressure that was nominally measured to be 15 atmosphere pressure, was made on the "clean gas system" in our main physics laboratory. The pressure was measured by a MKS Barotron manometer on the gas system. Since the phantom cell pressure was important for the subsequent polarimetry of polarized xenon gas. We tried to cross calibrate the xenon phantom gas density and pressure by water signal.

We used xenon calibrations obtained from the ~84 cm position, which was the most homogeneous part. Parameters for cross calibration of ^{129}Xe phantom cell density by water (^{1}H) signals were listed in Table 3.2. Calculated ^{129}xenon density was 6.299E-4 mole/ml. For an enriched (86.2%) ^{129}Xe cell with $Xe:O_2$ ratio of 5:1, this was equivalent to a cell pressure of 21 atmosphere.

Table 3.2 Parameters for cross calibration of ^{129}Xe phantom cell density by water (^{1}H) signal.

	Xenon cell (^{129}Xe)	Water cell (^{1}H)
Experiment time and file name	20060813162105	20060719153002,3137,3235
Gyromagnetic ratio (γ) MHz/Tesla	11.777	42.576
Volume ratio	1.003	1.0
Normalized signal (Volt)	5.825E-7	3.70E-4
Density (mole/ml)	**result: 6.299E-4**	0.111

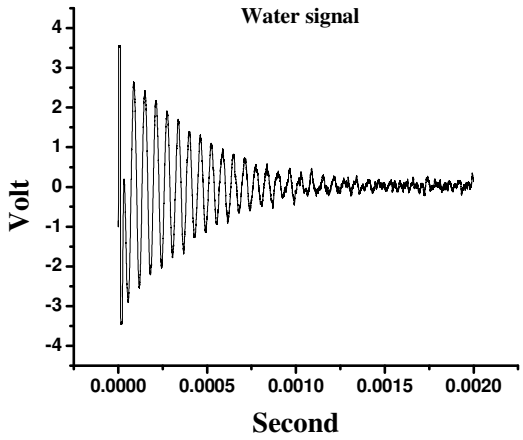

Fig. 3.6 Free induction decay (FID) of 2 cm water sphere cell in the electromagnet. The Lamor frequency was 11.921 MHz. 3 signal averaging by a computer. Total system amplification was17600 fold.

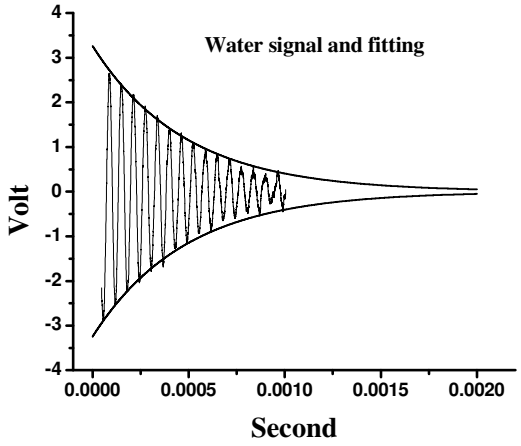

Fig. 3.7 Fitting of the peaks of free induction decay tracing. Peaks in Fig. 3.6 was selected and registered. These peaks data set were fitted with the equation y = amplitude x $\exp(-x/T_2^*)$. The fitting tracings of both upper part and lower part peaks were plotted and superimposed on the original tracing in the graph.

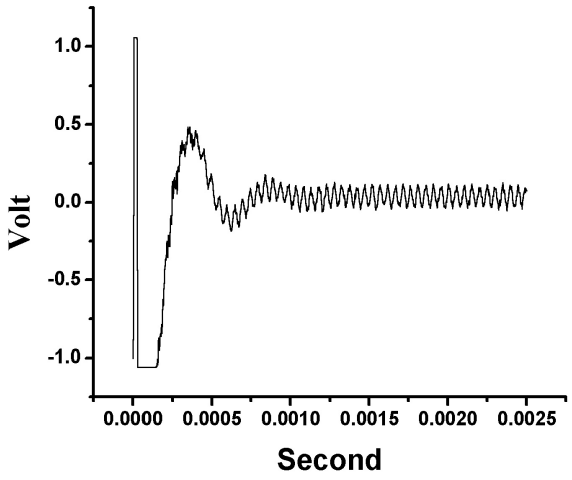

Fig. 3.8 FID tracings of enriched xenon sphere phantom cell at ~84 cm location of the10120 Gauss superconducting magnet. The Larmor frequency was 11.921 MHz. 256 signal averaging by a computer. Total system amplification was 257500 fold.

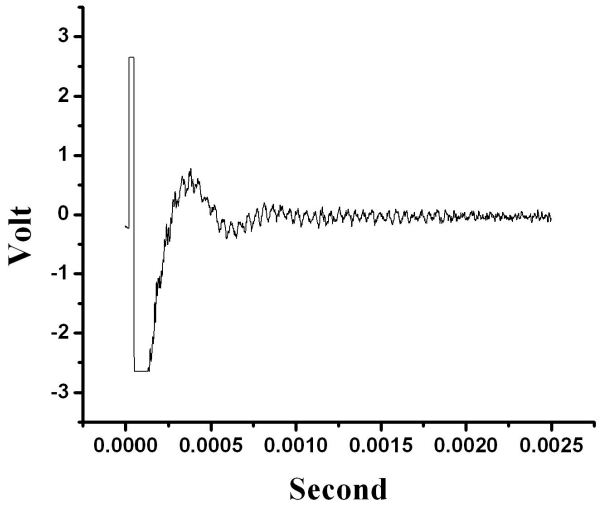

Fig. 3.9 FID tracings of enriched xenon sphere phantom cell at ~70 cm location of the10120 Gauss superconducting magnet. The Larmor frequency was 11.921 MHz. 64 signal averaging by a computer. Total system amplification was 515000 fold.

3.4.5 Xenon cylinder phantom cell experiment with a Helmholtz coil in the superconducting magnet

To monitor the xenon polarization during spin-exchange optical pumping, a Helmholtz coil was built to enclose the pumping cell for real-time NMR measurements. For calibration, an enriched xenon (86.2% ^{129}Xe) cylinder phantom cell was made. The cell's dimensions were the same as the pumping cell, 3.6 cm in diameter and 7 cm in length. Xenon to oxygen ratio was 5 to 1. Cell pressure was 4864 torr at 20 ^{0}C. The function generator was set to a frequency of 11.921 MHz, an amplitude of 950 mV, a pulse duration of 1.2 msec and was pulsed every 2 minutes. The computer was used to accumulate and average 510 signals. Total system amplification equaled 1030000 fold from the probe to the oscilloscope.

As shown in the upper graph of Fig. 3.10 was the FID tracings of the enriched xenon cylinder phantom cell. Because of huge amplification, the signals were mixed with initial coil and amplifier ringings. However, small xenon signals were noted after ~750 μsec. To process the signals, the first 630 μsec part of the original signal was truncated to discard the coil ringings. The signal tracings after truncation was Fast-Fourier - Transformed and the xenon signal peak showed up at the right frequency of 20.5 KHz.

Since the Helmholtz coil has less homogeneous B_1 field than the solenoid coil, the signal is much weaker. We tried hard to obtain one successful signal as shown in Fig. 3.10. We used this calibration consistently to measure the xenon polarization inside of the pumping cell. From the experiences of many experiments, this calibration was a reasonable value by reverse-estimation from the thawed-out xenon polarization which was calibrated by the more accurate small solenoid probe, while the calibration of the

small solenoid probe was described in section 3.4.1 to 3.4.4. The Helmholtz coil turned out to be very useful in measuring relative pumping cell polarizations under different conditions such as temperatures, flow rates and magnetic fields to find the optimal condition for operating the xenon gas polarizer.

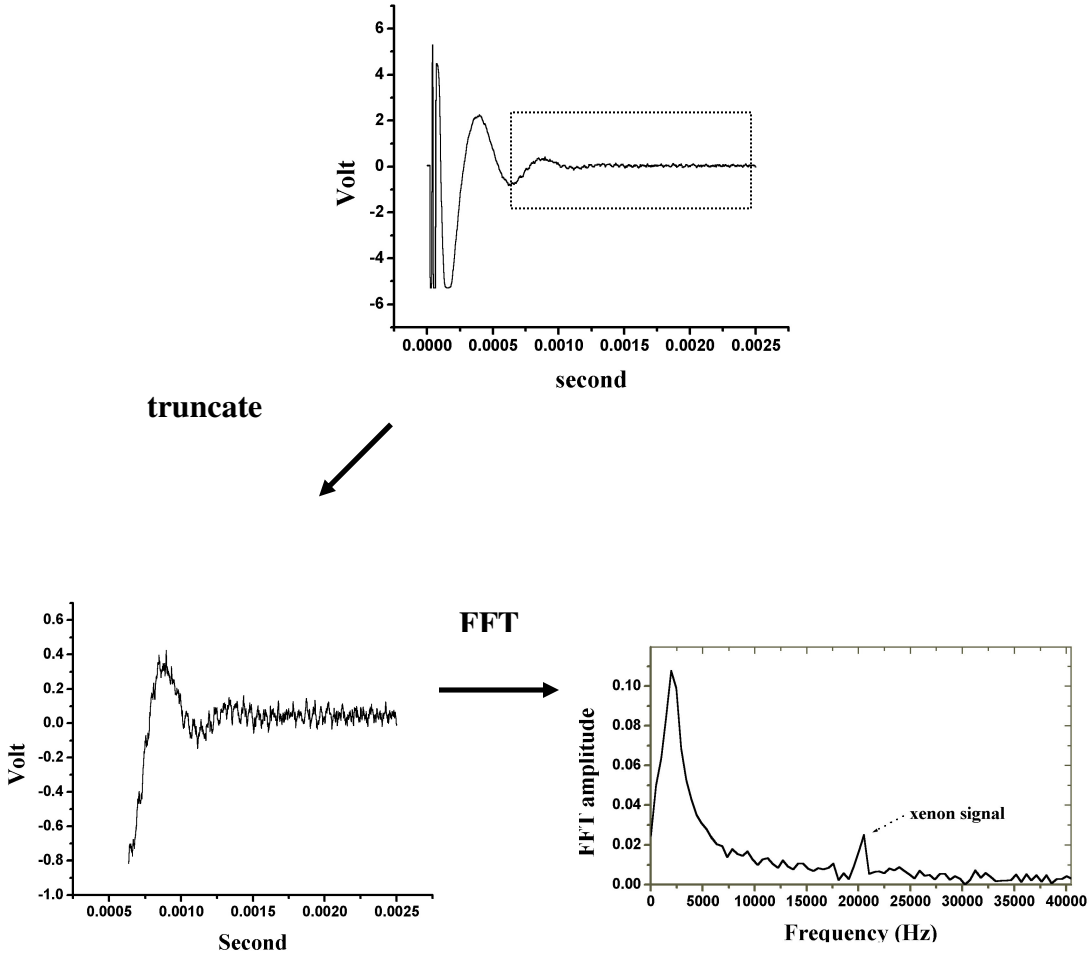

Fig. 3.10 FID tracings of enriched xenon cylinder phantom cell at ~84 cm location of the10120 gauss superconducting magnet. The NMR signal was obtained from a Helmholtz coil that enclosed the cell. The Larmor frequency was 11.921 MHz. 510 signal averaging by a computer. Total system amplification was 1030000 fold. A) Because of huge amplification, the signals were mixed with initial coil and amplifier ringings. Small xenon signals were noted after ~750 μsec. B) The first 630 μsec part of the original signal was truncated to discard the coil ringings. The Y-axis scale was enlarged. C) The signal tracings after truncation was Fast Fourier Transformed and shown in the lower right hand graph. Xenon peak showed up at the right frequency of 20.5 KHz.

3.4.6 More information on calibration

Since the accuracy of the calibration is determined by the total amplification fold. We further describe the related methods that we used.

The total system amplification was determined by injecting a small 1 mV sinusoidal signal into the ¼ wave-line and measuring the voltage output on the oscilloscope screen.

The second stage amplifier was made by Stanford Research with model number SR-560. It played a major role in determining the total amplification of the NMR system. The linearity graphs of the second stage amplifiers from physics laboratory and medical research building #4 are shown in Fig. 3.11. The R value is greater than 0.9999 and the P value is less than 0.0001 at each location.

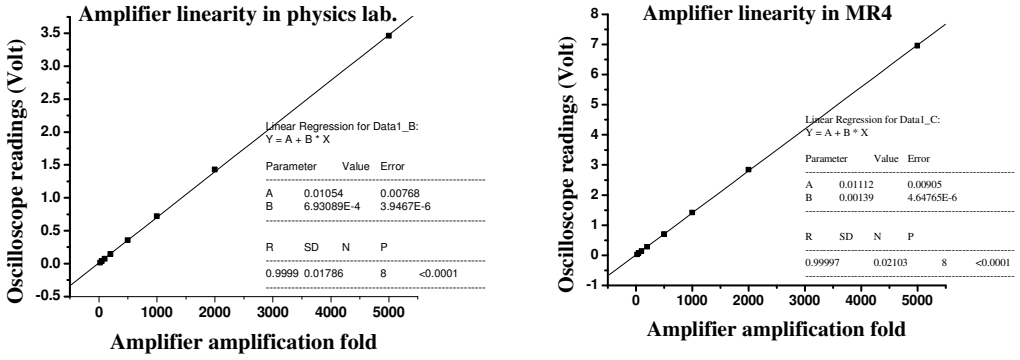

Fig. 3.11 Amplifier linearity. left) in physics laboratory, right) in medical-research building #4 (MR4). A 1 mV, 20 KHz sinusoidal signal was injected into a Standford Research SR560 amplifier, then the amplification fold was increased step by step and the output was measured by a Tektronix TDS3000 or TDS1002 oscilloscope. The R value is greater than 0.9999 and the P value is less than 0.0001 at each location.

Chapter 4 Optics and line narrowing of diode laser

4.1 Introduction

The rubidium D_1 transition line has a wavelength of 794.76 nm. Historically tunable Ti:Sapphire lasers or dye lasers have been used in noble gas optical pumping applications to match the narrow absorption width. The rapid development of high-power diode lasers which are relatively low-priced has shifted the use to diode lasers globally. However, the common spectrum width of a high-power diode laser is 2-4 nm FWHM. Elevating the pumping cell pressure increases the rubidium absorption spectrum width by pressure broadening (Ottinger et al. 1975). At 3572 torr (1% Xe, 10% N_2, 89% ^{4}He), the broadening is about 85 GHz (0.18 nm), and the shift is about 14 GHz (-0.03 nm)(Table 4.1, Romalis et al. 1997). This pressure-broadened absorption width of ~0.2 nm is still much less than the laser's FWHM of ~2 nm. A line-narrowed diode laser spectrum usually has a FWHM of 0.2 nm. This is comparable with the width of the pressure-broadened absorption trough (Chann et al. 2000). We tested both injection locking and external cavity methods to narrow the diode laser spectrum and found greatly improved performance.

Table 4.1 Rubidium D1 line pressure broadening and line shift (Romalis et al. 1997)

	^{4}He	N_2	Xe
D_1 full width GHz/amg.	18.0±0.2	17.8±0.3	18.9±0.5
D_1 line shift GHz/amg.	4.3±0.1	-8.25±0.15	-5.05±0.3

Note: amg = ideal gas density at 0 ^{0}C and 760 torr.

4.2 Monochromator

A Jobin Yvon Triax_550 monochromator was used in our physics main laboratory for experiments of injection locking and external-cavity line narrowing. This monochromator has a two dimensional CCD and a photomultiplier. The resolution is 0.01 nm.

An Ocean Optics HR-4000 portable spectrometer was used in the new xenon polarizer set-up in medical research building #4. Its resolution is 0.1 nm.

4.3 Injection-locking line narrowing

To understand the behavior of diode laser line narrowing, we first used a precision tunable Ti:Sapphire laser to line narrow a 1 watt diode laser. The FWHM of Ti:Sapphire laser was less than 1×10^{-6} nm. This light was directed to shine on the emitter of the 1 watt diode laser. Output light was sampled by a beam-splitter for spectrum analysis (Fig. 4.1). The FWHM of the narrowed light was ~0.1 nm, while FWHM of the unnarrowed laser light was ~1 nm (Fig. 4.2). The disadvantage of injection locking is that it requires an expensive Ti:Sapphire laser as a master laser. Using single frequency diodes could be an alternative, but the power output is also small. Furthermore, it is hard to apply injection locking to a diode laser bar.

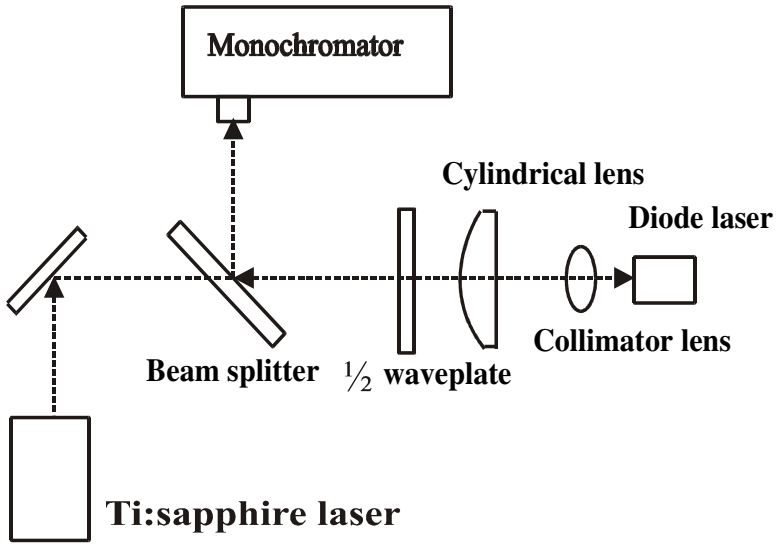

Fig. 4.1 Injection locking of 1 watt diode laser. The light of tunable Ti:sapphire laser was directed to shine on the diode laser emitter for injection locking. The ½ waveplate was used to rotate the polarization axis. A collimator lens and a cylindrical lens served as beam shaping optics for the diode laser. The output light was directed to a monochromator for spectrum analysis.

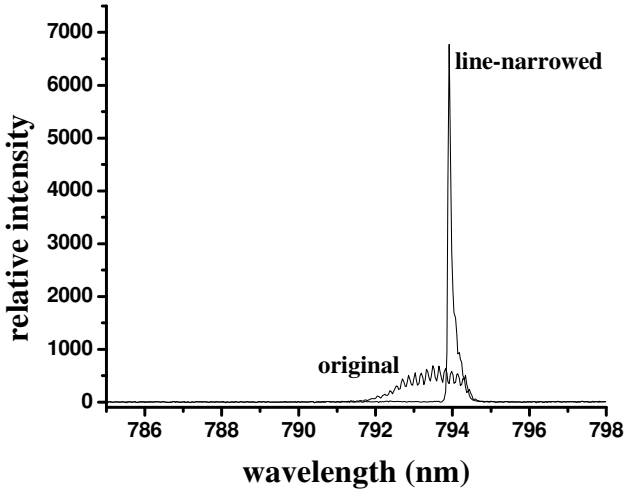

Fig. 4.2 Diode laser output spectrum before and after injection locking. The short broad spectrum was before injection locking, FWHM ≅ 1nm. The tall spike was after injection locking, FWHM ≅ 0.1 nm.

4.4 External cavity line narrowing

A more successful configuration involved the use of a high-power diode laser array together with a diffraction grating which was used to create an external cavity.

The high-power diode bar was temperature-controlled by a recirculating and deionizing water chiller. The bare diode laser bars that we used had 25 small emitters. Each emitter's dimension is 200 μm X 100 μm. The emitter pitch is 400 μm. Total distance is 1 cm (Fig. 4.3). For a typical diode laser, the vertical (fast) axis divergence was ~30 degree, (which is a diffraction phenomenon because the small vertical dimension is comparable to the wavelength of the light). The horizontal (slow) axis divergence was ~5 degree. A fast axis microlens reduced this axis' divergence to ~1 degree. The diode laser and a holographic grating were put in a Littrow configuration. A telescope lens combination enlarged the slit dimension by a factor of 4. The first-order diffracted light from the holographic grating was arranged to reflect back onto the diode laser itself. This created the external cavity between the diode laser and the grating. Some resonant photon energy resided within the cavity. The zero-order diffracted light from the grating was the output light that was coupled to a pumping cell (Fig 4.4, Chann et al. 2000). Before narrowing, the diode laser's power output was 52.5 watt and the FWHM was 2.5 nm. After narrowing, the power output was 44 watt and the FWHM was 0.17 nm. (Fig. 4.5)

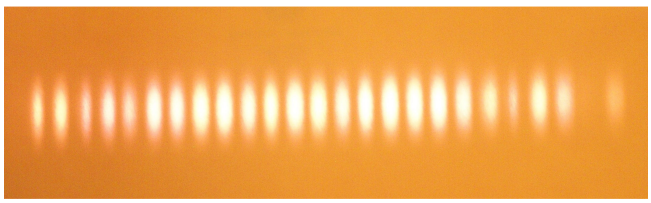

Fig. 4.3 Emitter profiles of high-power diode array bar. Each emitter is 200 μm X 100 μm. The pitch is 400 μm. A total of 25 emitters span 1 cm.

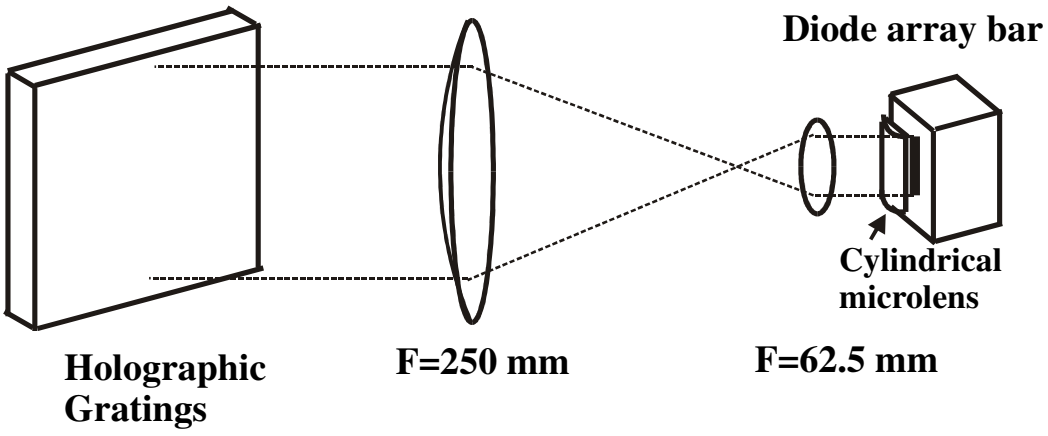

Fig 4.4 External cavity line narrowing in a Littrow configuration. The high-power diode laser array had a small fast-axis microlens for easy collimation. The beam-expanding telescope lens comprised of a 62.5 mm and a 250 mm lens. It enlarged the laser light by 4 fold prior to shining on a holographic grating. First order diffracted light was aligned to shine backward onto the diode laser, while zero order diffraction light was used as output light (Chann et al. 2000).

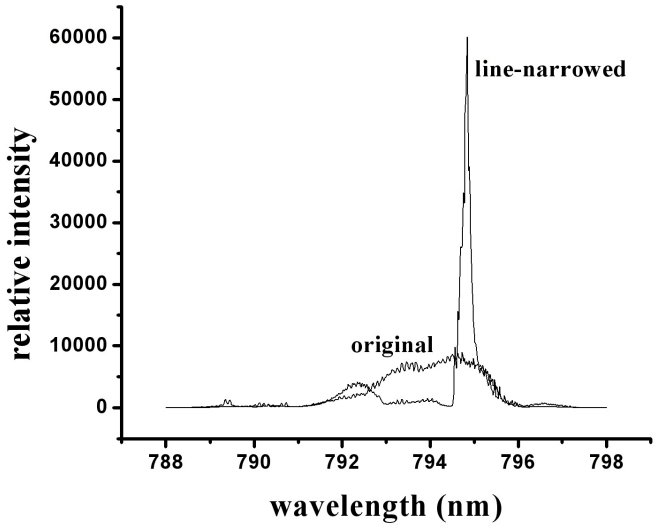

Fig. 4.5 High power diode laser output spectrum before and after external cavity line narrowing. The short broad spectrum was before narrowing, FWHM = 2.5 nm. The tall spike was after narrowing, FWHM= 0.17 nm.

4.5 Two orthogonal line-narrowed diode laser

4.5.1 Introduction:

The two dimensional light intensity profile of a diode laser bar is like a ridge with Gaussian cross section pattern (Fig. 4.6 A). Since the ridge intensity is higher than the slope's, inhomogeneous light intensity will decrease the efficiency of an optical pumping. A light diffuser can smooth the laser light to make it more homogeneous. Unfortunately, it also reduces the laser power by about 8-10%. To compensate for this problem, an additional line-narrowed diode laser was added to the set-up. This had two advantages. Firstly, it increased the light intensity. Secondly, it homogenized the light output.

4.5.2 Simulation

To better understand the effect of combining the light from two bars, a Matlab program was written. Two configurations of the diode laser arrays were simulated. One in which the axes were parallel, and one in which the axes were orthogonal. We could also specify the position of the centroid of each bar's distribution with respect to the other. As shown in figure 4.6 C, the combination of two parallel Gaussian ridges add up to be a larger Gaussian beam. When the centroids of the two beams are moved apart, there is a central plateau just like the intervening magnetic field in a Helmholtz coil. We lose more laser light if the two centroids are too far apart, even though its homogeneity will increase. As shown in the figure 4.6 B, it is evident that the orthogonal configuration gave better homogeneity and less loss of laser light. The intensity histograms of both configurations are presented in Fig. 4.7. The orthogonal configuration has larger total and mean intensity and smaller standard deviation in intensity distribution (Table 4.2).

A

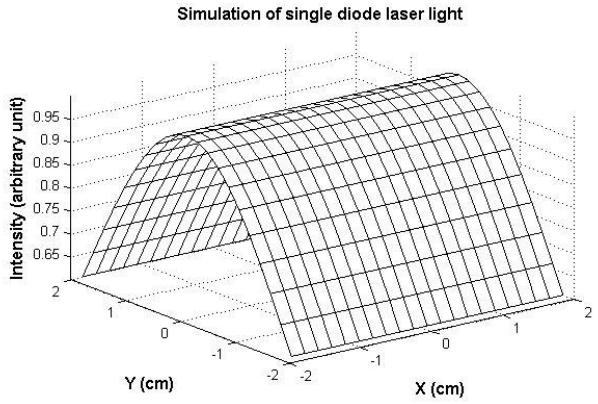

B

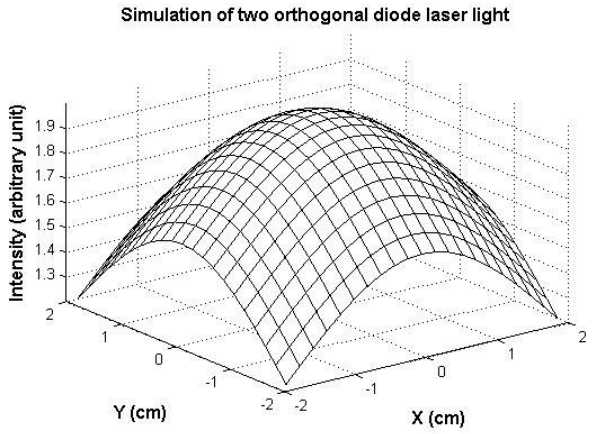

C

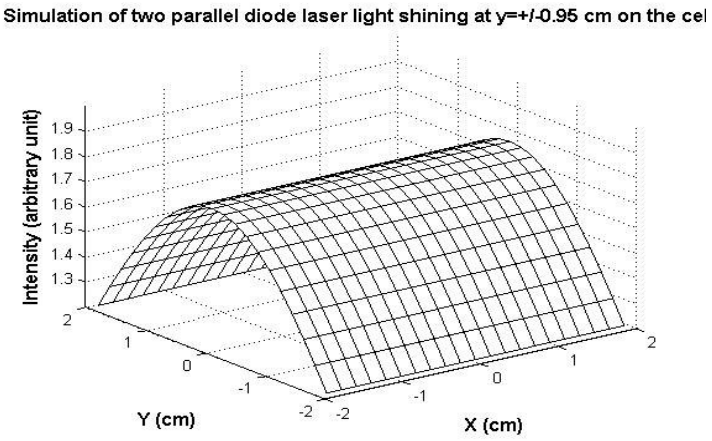

Fig. 4.6 Simulation of diode laser shining on a 4 X 4 cm target. Intensity is in relative units. A: Single diode laser, B: Two orthogonal diode lasers, C: Parallel diode lasers with light ridge at y = +/- 0.95 cm.

A

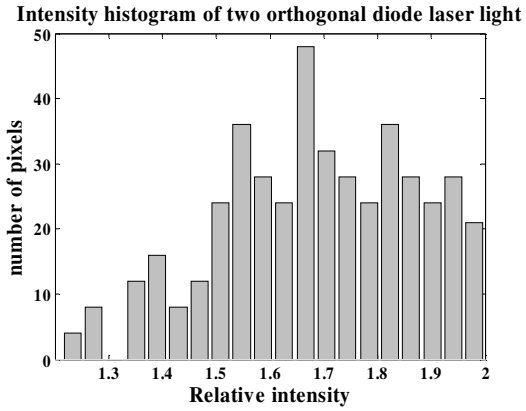

B

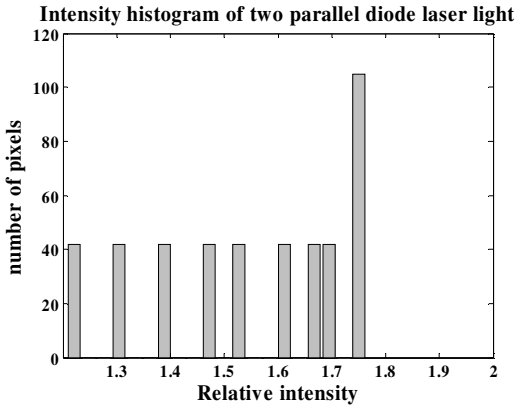

Fig. 4.7 Intensity histogram of diode laser light A) Two orthogonal configuration, refer to Fig. 4.6 B, B) Two parallel configuration, refer to Fig. 4.6 C.

Table 4.2 Statistics on simulation of pixel intensity

	Two orthogonal	Two parallel with both light ridges at y= 0.0 cm	Two parallel with light ridges at y= ± 0.95 cm
Sum	743.8	743.8	682.7
mean	1.69	1.69	1.55
Standard deviation	0.185	0.262	0.185

4.5.3 Beam shaping:

To couple the rectangular distribution of diode laser light to the pumping cell and to reduce power loss during transport through optical components, beam shaping optics were designed which improved upon published configurations from other groups. Firstly, cylindrical lenses were used for both fast and slow axis beam shaping. This increased the ease with which the beam could be shaped in two dimensions. Also, the use of a concave cylindrical lens saved bench space. To reduce the number of optical components, a single converging lens was used as the last lens for both axes. (Fig. 4.8)

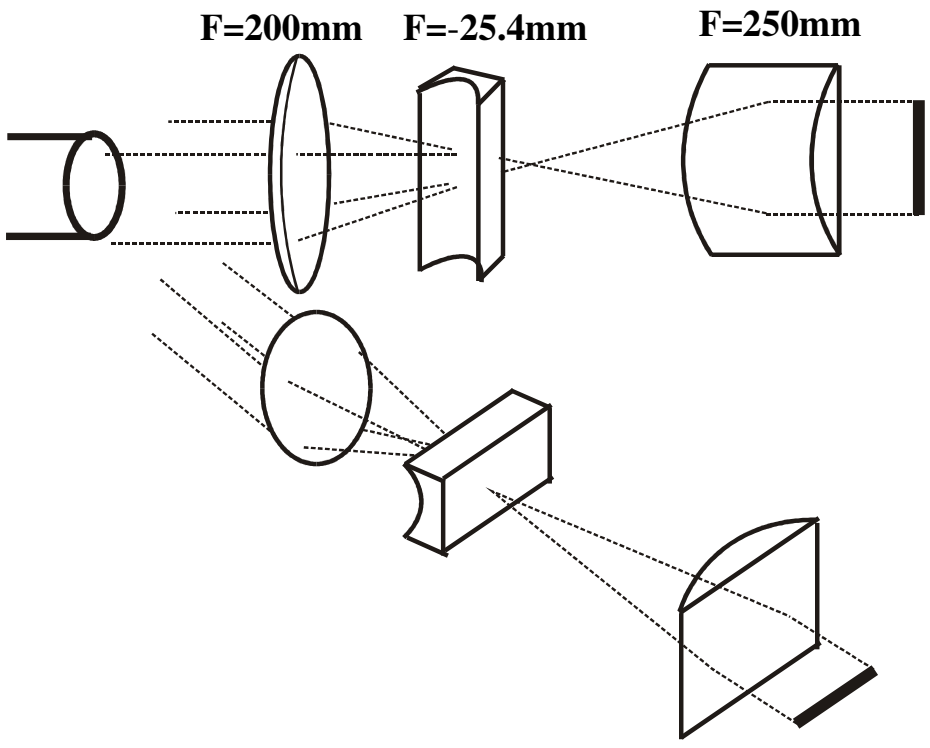

Fig. 4.8 Two orthogonal and two axes beam shaping optics. Telescope lenses combinations were applied to both fast axis and slow axis. Individual cylindrical lens was used to increase the ease in coupling beams to pumping cell at the left end.

4.5.4 Optical pumping experiment, results and discussion

To investigate the efficacy of the orthogonal-axis geometry, several tests were performed in which xenon was polarized using different laser configurations. In one case an orthogonal axis geometry with a combined power of 37 watts was compared to a single diode laser operating at 40 watts. The results of this test are shown in Fig. 4.9. For each configuration, temperature was also scanned to find the optimal operating point. With two orthogonal diode lasers operating at combined power of 37 watts, the xenon polarization was higher than a single diode laser operating at 40 watts. This could be interpreted as two orthogonal diode lasers are more homogeneous than single diode laser (Fig.4.9).

In another test, two orthogonal diode lasers with a combined power of 70 watts were compared to each single diode laser operating at 30 watts and 40 watts. The results of this test are presented in Fig. 4.10. Diode laser #1 operating at 30 watts had maximal signal strength of 1.1 near 90 ^{0}C. Diode laser #2 operating at 40 watts had maximal signal strength of 1.15 near 100 ^{0}C. Two orthogonal diode lasers #1 & #2 at combined power of 70 watts had maximal signal strength of 1.61 at 85 ^{0}C(Fig. 4.10). This showed non-linear incremental of polarization with two orthogonal laser light. We interpreted this as that the laser light was approaching its maximal effect on polarization with two diode lasers, though there was still room for further laser power. To reach even higher polarization, we also need to improve other limiting factors such as the relaxation characteristics of the pumping chamber or spin-exchange efficiency. Furthermore, the optimal oven temperature of the two-laser experiment was lower than that of individual laser

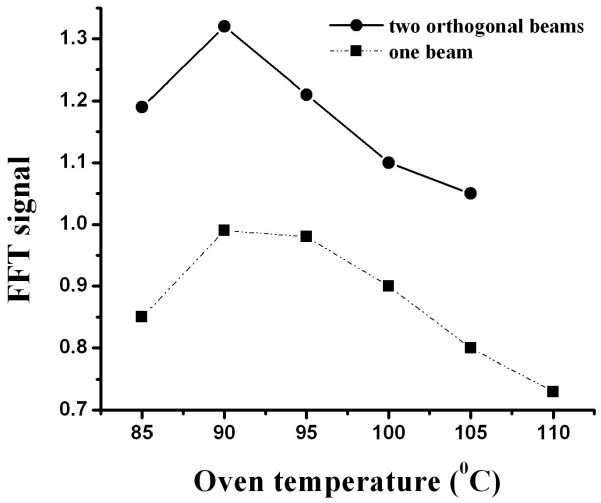

Fig. 4.9 Temperature scanning of xenon polarization with two orthogonal diode lasers and single diode laser. Circle: two orthogonal diode lasers operating at 37 watts. Square: single diode laser operating at 40 watts. Note: cell temperature may be 20~30 ^{0}C higher than oven temperature.

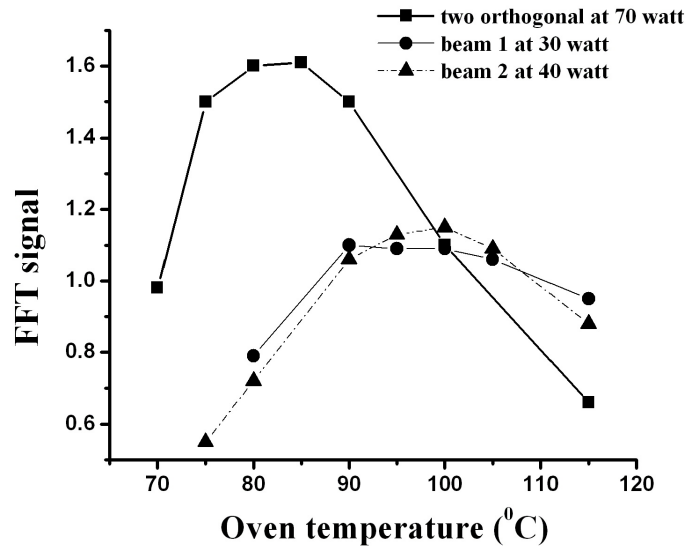

Fig. 4.10 Temperature scanning of xenon polarization with two orthogonal diode lasers and individual diode laser. Square: two orthogonal diode laser operating at 70 watts. Circle: diode laser #1 operating at 30 watts. Triangle: diode laser #2 operating at 40 watts.

experiment. We interpreted this as that two diode lasers had larger heating effect on pumping cell. Higher interior temperature led to denser rubidium vapor. The apparent oven temperature might not reflect the true temperature inside of the cell.

We have developed two orthogonal line-narrowed lasers configuration for spin-exchange optical pumping. This set-up improved the homogeneity of the laser light and increased the total power output. Optical pumping with two diode lasers increased xenon polarization. Both lasers were powered by the same laser driver and cooled down by the same water chiller. This configuration was cost-effective.

4.6 Centering diode laser spectrum

As the diode laser was line narrowed, the spectrum FWHM was near ~0.2 nm. Adjusting the spectrum central line to match the rubidium D1 absorption trough became even more important than in a diode laser without line narrowing. A high-resolution spectrometer and magnetic resonance signals were both used as feedback methods for centering the spectrum.

4.6.1 Absorption spectrum measurement:

A fiber was placed at the back of the pumping cell. As un-narrowed diode laser light passed through the cell, the spectrum was measured when the oven was at room temperature (Fig. 4.11) and at 100 ^{0}C (Fig. 4.12). When the room-temperature spectrum is subtracted from the 100^{0}C spectrum, the "difference spectrum" shown in Fig. 4.13 is obtained, which clearly shows the Rb absorption line at 794.76 nm. For these data the gas pressure was Xe 72 torr, N_2 357 torr, and ^{4}He 3143 torr.

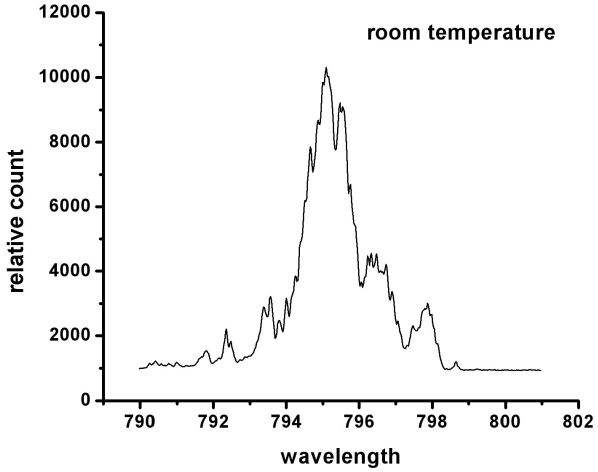

Fig. 4.11 Un-narrowed laser absorption spectrum at room temperature (23 ^{0}C)

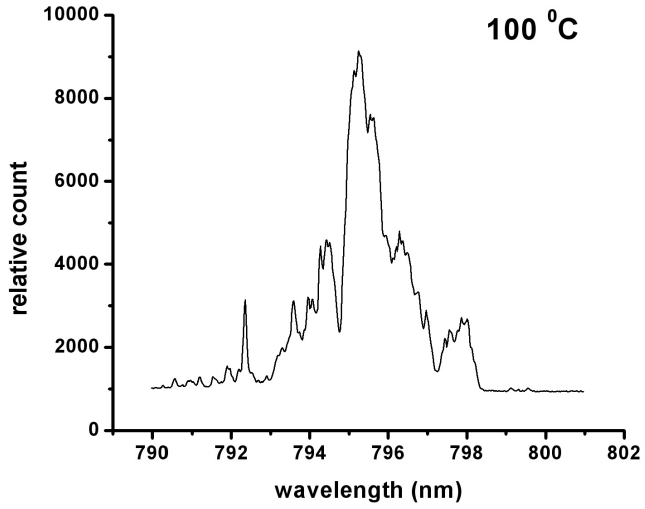

Fig. 4.12 Un-narrowed diode laser absorption spectrum at oven temperature of 100 ^{0}C.

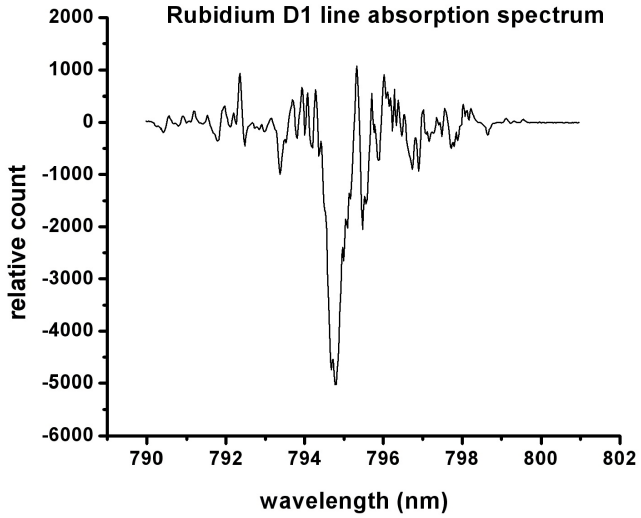

Fig. 4.13 Subtracted absorption spectrum of un-narrowed diode laser (Fig. 4.12 – Fig. 4.11). FWHM extended from 794.6 nm to 795 nm. The maximal absorption was near 794.76 nm, which agreeed with the previous graph.

4.6.2 NMR experiment:

In a separate test, optical pumping was performed at different wavelength**.** NMR signal from the polarized xenon was measured to investigate the wavelength effect on final polarization.

Spin-exchange optical pumping with line-narrowed diode laser was done with gas pressure of Xe 72 torr, N_2 357 torr, and ^{4}He 3143 torr (at room temperature) and heated up to 100 ^{0}C. Each pumping duration was 4 minutes. As shown in Figure 4.14, the optimal point was around 794.75 nm, which was very close to the 794.76 nm in spectrum absorption graph (Fig. 4.13). Furthermore, near the center point, a little off target in wavelength selection had no significant effect on the NMR FFT signal strength. Experiments on 1% xenon gas mixture were also conducted with similar results.

When the peak wavelength of line-narrowed laser light was varied, the laser collimation and coupling to the pumping cell was also changed. Compensation adjustment was done in each movement of wavelength. Judging from the experiment result, the small coupling variation had no significant effect.

4.6.3 Discussion and Conclusion on line centering

Both absorption spectrum analysis and NMR signals of direct optical pumping showed compatible results. The absorption peak was at 794.76 nm when the gas pressure was Xe 72 torr, N_2 357 torr, and ^{4}He 3143 torr. The FWHM of absorption trough was ~0.4 nm which covered the line-narrowed laser spectrum FWHM of ~0.2 nm. This finding was also confirmed in NMR measurement that a little off-target from 794.75 nm had no significant effect on final polarization.

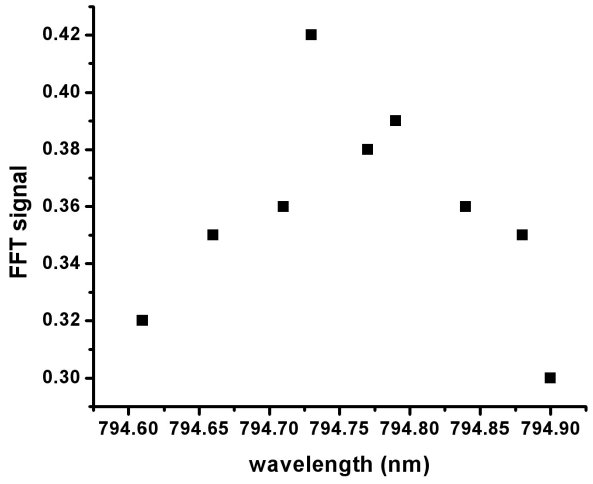

Fig. 4.14 Fourier transform of FID signals from spin-exchange optical pumping using line-narrowed diode laser at different center wavelengths.

Chapter 5 Xenon polarizer characterization and magnetic field studies

We introduced the spin-exchange rate constant γ', and cell wall relaxation rate Γ_{Xe} in Chapter 2. We know that they play important roles in affecting our final xenon polarization. As the system was operated in 10120 gauss field, we were interested in investigating the magnetic field effect on spin exchange rate. Furthermore, there was no published measurement of spin-exchange rate constant at our working gas composition, pressure and magnetic field. In this chapter, we will first introduce experiments on measuring γ' and Γ_{Xe} and compare results with published data. These experiments were done in closed-cell condition. Both glass valves of the cell were closed. We define this as static optical pumping.

Secondly, we describe control experiments by comparing the flowing xenon polarizations of cells located in different magnetic fields. Both glass valves were opened. Xenon mixture gas flew into the cell, was laser-pumped, and exited to the connecting tubing. We define this as continuous flow mode of operation.

Finally, we present complete xenon accumulation experiments at different magnetic fields. Exit gases from the pumping cell flew through a liquid nitrogen bath to accumulate xenon. We define this as the xenon accumulation mode of operation. This was to test the integral system performance in response to different magnetic fields.

5.1 Static spin-exchange optical pumping

To measure the spin-exchange rate constant γ', and cell wall relaxation rate $\Gamma_{Xe,}$ we conducted a series of static spin-exchange optical pumping tests of our pumping cells.

The results were compared to other published data with various gas compositions, pressures and at different magnetic fields.

5.1.1 Methods and Results

Experimental methods:

Spin up experiment at each specific temperature

Xenon cell was optically pumped in 10120 gauss field for studying cell spin-up kinetics. The cell was filled with rubidium and 2% xenon gas mixture at 2280-4560 torr. A Helmholtz coil inside the oven enclosed the cell for real time NMR measurement and monitoring. Before each pumping up experiment, the cell was irradiated with more than ten RF pulses to depolarize the residual xenon polarization inside of the cell completely. The cell was subsequently pumped for specific time duration. Finally, its polarization was measured by NMR (Fig. 5.1). This cycle was repeated with different pump-up time durations at the same temperature several times.

These spin-up polarization measurements were fit with the exponential growth equation:

$$P_{Xe} = P_{\max}[1 - e^{-t/T_1^*}] \tag{5.1}$$

We thus obtained the spin-up time constant T_1^* at one specific cell temperature.

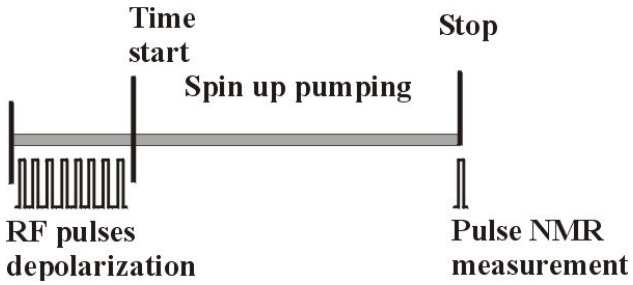

Fig. 5.1 Spin-up experiment. Before each spin-up experiment, the pumping cell was irradiated with more than 10 RF pulses to depolarize it completely. Afterwards, the pumping up process proceeded with specific time duration. Pulse NMR measurement was applied at the end. The whole cycle was repeated with different pumping up duration at the same temperature for several times. NMR signals could be plotted for exponential growth curve fitting (equation 5.1).

Linear fitting of $1/T_1^*$ and [Rb] with equation 5.2

A series of spin-up experiments were performed at different temperatures. At each temperature we measured its corresponding T_1^*. The rubidium density [Rb] could be estimated by the empirical Killian formula from temperature measurement (Killian, T. 1926):

$$[Rb] = \frac{10^{-7} \times (10^{(10.55 - \frac{4132}{T})})}{k_B T} (\frac{atom}{cm^3}) \tag{5.2}$$

where T is temperature in Kelvin, and k_B is the Boltzmann constant.

The inverse of T_1^*, $1/T_1^*$, was then plotted against [Rb]. This graph was linearly fit with:

$$\frac{1}{T_1^*} = [Rb]\gamma' + \Gamma_{Xe} \tag{5.3}$$

where γ' is the spin-exchange rate constant which includes contribution from van der Waals interaction and binary collisions ($\langle \sigma v \rangle_{SE}$) and Γ_{Xe} is the xenon wall relaxation rate. From the fit line, the line slope was $\gamma_{\cdot}$, and the intercept was Γ_{Xe} (Cates, et al. 1992).

Results:

Fig. 5.2 shows a series of spin-up experiments on cell#1 at $Xe/N_2/^4He$ pressure of 43/216/1899 torr. Experiments were run on 75, 87.5, 100, 115 and 130 ^{0}C separately. Exponential fitting of T_1^* from each temperature were then used to plot $1/T_1^*$ vs. [Rb] plot as shown in the first graph labeled 20051021 of Fig. 5.2. The slope was measured to be 3.87 x 10^{-16}cm^{3}sec^{-1}, which was the spin-exchange rate constant $\gamma_{\cdot}$. The intercept was 0.00358 sec^{-1}, of which the inverse was 279 seconds, which was the intrinsic wall relaxation time constant of the #1 cell.

Fig. 5.3 shows the results presented in Fig. 5.2 as well as those from 6 other series of spin-up experiments. Exponential growth curves from each experiment are not shown to avoid redundancy. Only final linear fits are presented.

Details of the cell conditions, fitted values of $\gamma_{\cdot}$ and Γ_{Xe}, and the statistical significance are further listed in Table 5.1.

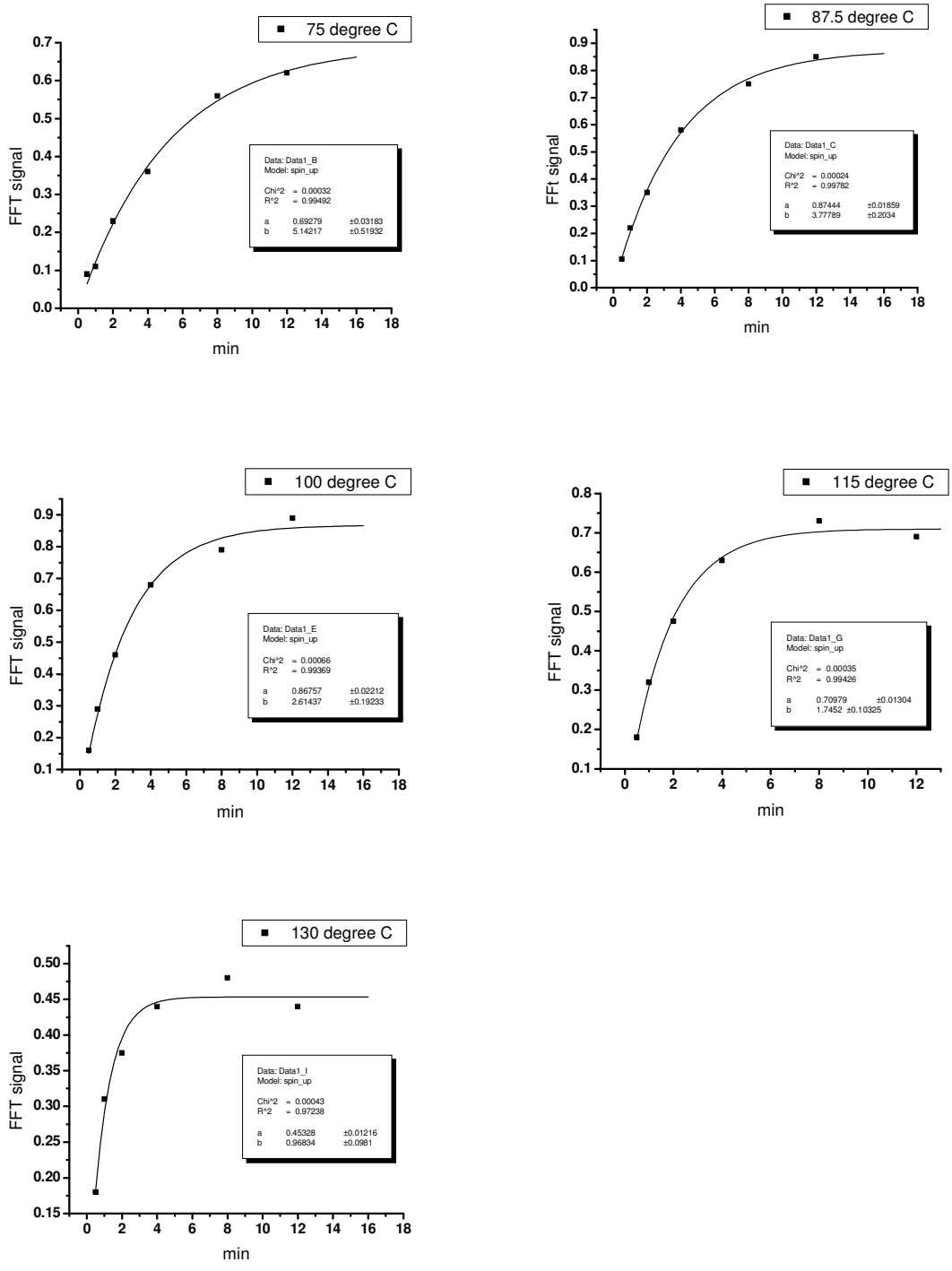

Fig. 5.2: Spin up experiments performed at 5 different temperature as indicated in each graph. The signal strength was fit with $P_{Xe} = P_{\max}[1 - e^{-t/T_1^*}]$ to obtain spin up time constant T_1^*. Experiment was done on Oct 21, 2005.

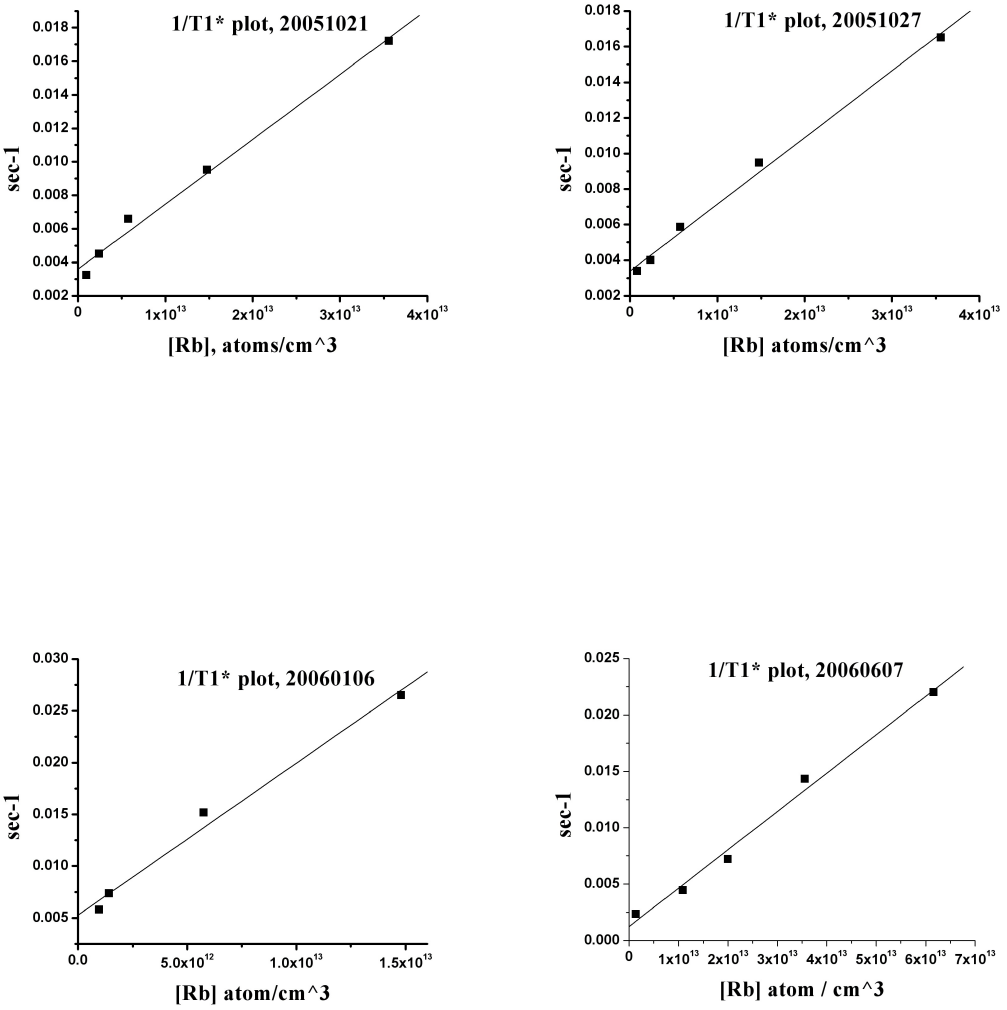

Fig. 5.3: Linear fitting graph of $1/T_1^*$ and [Rb]. Continued in next page.

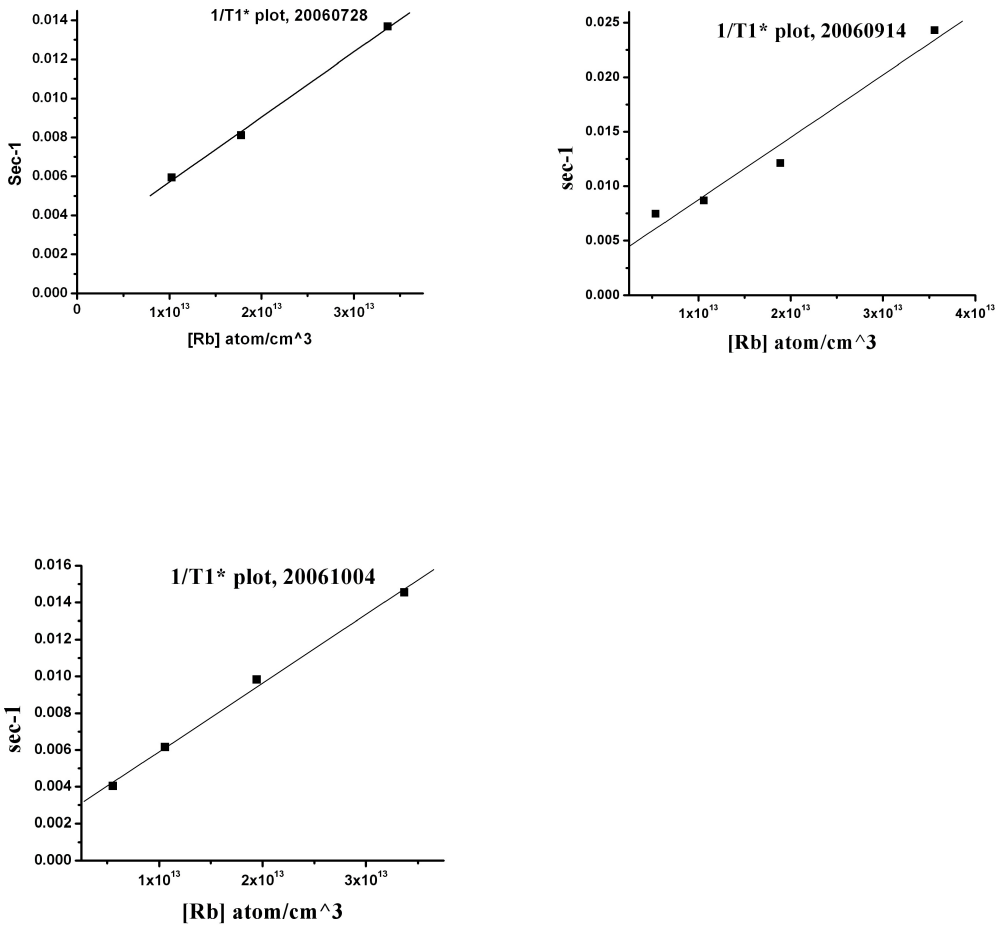

Fig. 5.3: Linear fitting graph of $1/T_1^*$ and [Rb]. T_1^* measured from 5 each temperature as shown in Fig. 5.2 were used to plot the $1/T_1^*$ vs. [Rb] graph located on upper-left of this figure, labeled 20051021. The graph was linearly fitted with the equation $\frac{1}{T_1^*} = [Rb]\gamma' + \Gamma_{Xe}$ to obtain the intercept Γ_{Xe} (wall relaxation rate) and the slope γ'(spin-exchange rate constant). The other 6 graphs were plotted similarly. Their exponential growth graphs were not shown to avoid redundancy. Experiment date was labeled in each graph. Refer to table 5.1 for detailed information.

Table 5.1: Summary of measurements at 10120 gauss:

	date	Condition: $Xe/N_2/^4He$ (torr) and RTD location	γ $(10^{-16}cm^3sec^{-1})$	Wall relaxation time constant (sec)	P value (10^{-4})
#1	20051021	43/216/1899 cell stump surface temperature	3.87 ± 0.22	279	4.07
#1	20051027	90/452/3979 cell stump surface temperature	3.75 ± 0.16	295	1.61
#1	20060106	90/452/3979 cell stump surface temperature	1.47 ± 0.11	190	58.6
refurbished #1	20060607	71/357/3143 cell body surface temperature	3.4 ± 0.19	806	3.62
refurbished #2	20060728	36/365/3247 cell body surface temperature	3.33 ± 0.15	422	278.3
loop #1	20060914	36/365/3247 cell body surface temperature	5.72 ± 0.74	330	165
loop #2	20061004	36/365/3247 cell body surface temperature	3.73 ± 0.16	461	19.1

Note: Pressure measured at room temperature of 23^0C.

5.1.2 Discussion

Cates et al.(1992) reported $\gamma_{\cdot}$ of 5.48 ±0.08 x 10^{-16}cm^{3}sec^{-1}, with a van der Waals spin-exchange rate of 1.78 x 10^{-16}cm^{3}sec^{-1}, and a binary collision rate $\langle \sigma v \rangle_{SE}$ of 3.7 ±0.15 ±0.55 x 10^{-16}cm^{3}sec^{-1} in a cell containing Xe/N_2 pressure of 843/49 torr at 0.11 gauss condition. We measured the combined spin-exchange rate constant $\gamma_{\cdot}$ in 7 series of experiments at 10120 gauss. One of the pumping cell with a gas composition of Xe/N_2/^{4}He at the pressure of 71/357/3143 torr, which was similar to the Xe/N_2 pressure of 843/49 torr in breaking up van der Waals molecules, was tested and the measured $\gamma_{\cdot}$ was 3.4 ± 0.19 x 10^{-16}cm^{3}sec^{-1}. Our measured $\gamma_{\cdot}$ was similar to the $\langle \sigma v \rangle_{SE}$, as measured by Cates et al.(1992). We have reviewed in section 2.2 that magnetic field of ~hundreds gauss slow down van der Waals process. This suggested that van der Waals interaction was turned off in our pumping cell at 10120 gauss (Table 5.2). What factors turned off the van der Waals process in our cell, the 3648 torr pressure, 10120 gauss field, or both?

What is the status of van der Waals process in a cell with similar gas composition, and pressure as our cell but under ~10-20 Gauss field? This is the condition of most xenon polarizer, for example, the MITI polarizer in the Radiology Department of University of Virginia. It was reported that N_2 and ^{4}He were less destructive to van der Waals process than xenon (Shao et al. 2005, Cates et al. 1992, Rice and Raftery 2002). The weighting was 0.275 for N_2 compared to xenon. Since ^{4}He's cross section is smaller than N_2, we can also approximate ^{4}He's weighting to be 0.275(Rice and Raftery 2002). For our pumping cell of Xe/N_2/^{4}He pressure of 71/357/3143 torr, this was equivalent to ~950 Torr of xenon effect. Compared to Cates et al.(1992)'s cell condition with xenon pressure of 843 torr or 1817 torr, our pumping cell should have some van der Waals

process at ~10-20 gauss (Table 5.2). Putting our pumping cell in 10120 gauss field might further slow down van der Waals interaction.

Chann et al. (2002) identified a new gas-phase, room temperature spin-relaxation mechanism due to spin-rotation coupling in bound Xe-Xe van der Waals molecules. They reported that ^{4}He was ¼ fold less in strength compared to N_2 in breaking up the Xe-Xe van der Waals complex. This give us a hint that even though the xenon gas mixture used in MITI version of polarizer has a pressure of 3648 torr, however, 89% of it is ^{4}He, which is a weak van der Waals breaker notoriously. The van der Waals process might still play a significant role for MITI polarizer which is at low field condition.

Reduced spin-exchange rate at high magnetic field will increase T_1^*, the spin build-up time constant, since $1/T_1^*$ equaled spin-exchange rate plus wall relaxation rate (equation 5.3). In our case of 10120 gauss field, for static spin-exchange pumping, T_1^* lengthening had no worse effect on our final xenon polarization so long as we pumped it longer time. However, in continuous flow operation, the xenon transit time was limited by the flow rate and the chamber length. Xenon would have not enough time to build up polarization if T_1^* was prolonged. The outlet xenon polarization would decrease. On the contrary, decreased wall relaxation at high magnetic field will increase the outlet xenon polarization, and this is always welcomed. We will investigate this subject in the next section.

Table 5.2 . Comparison of spin-exchange rate. (Rice and Raftery, 2002)

	Gas mixture	Pressure (torr)	B_0 (gauss)	T_{wall} (min)	γ' (10^{-16} cm^3s^{-1})	van der Waals (10^{-16} cm^3s^{-1})	$\langle \sigma v \rangle_{SE}$ (10^{-16} cm^3s^{-1})
Cates	Xe/N_2	245/49	0.11	9.6	9.9	6.2	3.7
Cates	Xe/N_2	350/53	0.11	7.4	8.3	4.6	3.7
Cates	Xe/N_2	843/49	0.11	5.4	5.5	1.8	3.7
Cates	Xe/N_2	1817/50	0.11	3.9	4.9	1.2	3.7
Zeng	Xe/N_2	1/23	5	--	90.6	86.5	4.1
Zeng	Xe/N_2	1/35	5	--	71.3	67.2	4.1
Zeng	Xe/N_2	1/56	5	--	52.5	48.4	4.1
Zeng	Xe/N_2	1/96	5	--	30.4	26.3	4.1
This work (Wang)	Xe/N_2/He	43/216/1899	10120	4.9	3.87	--	--
This work (Wang)	Xe/N_2/He	71/357/3143	10120	13.4	3.4	--	--
Xeng	Xe/N_2	15/55	18790	12	5.1	--	--
Zilm	Xe/N_2	450/50	23500	330	2.8	--	--
Zilm	Xe/N_2	1500/76	23500	69.4	7.4	--	--
Liu	Xe/N_2	15/55	47000	7	6.3	--	--
Rice	Xe/N_2/He	72/60/303	47000	170	2.0	1.4	0.6
Rice	Xe/N_2/He	72/60/532	47000	130	1.4	0.80	0.6
Rice	Xe/N_2/He	72/60/976	47000	42	1.0	0.40	0.6
Rice	Xe/N_2/He	72/60/1328	47000	43	0.93	0.33	0.6
Rice	Xe/N_2/He	72/60/1654	47000	31	0.86	0.26	0.6
Jau[a]	Xe	600	94000	--	1.76	--	--
Jau	Xe	3040	94000	--	1.78	--	--
Jau	Xe/N_2	600/760	94000	--	1.60	--	--
Jau	Xe/N_2	600/2280	94000	--	1.84	--	--

a: Jau et al., 2002.

5.2 Continuous flow xenon optical pumping in different magnetic field

5.2.1 Introduction:

To investigate the effect of magnetic field on spin-exchange optical pumping, xenon continuous flow experiments were performed in different locations inside and around the

magnet. These represent the conditions that we use when accumulating xenon for imaging experiments. For these studies, however, we did not accumulate the gas. Among other things, this allows us to separate any possible losses due to accumulation.

5.2.2 Materials and Methods:

To test the effect of different magnetic filed strengths on the polarization, the pumping cell was placed at various positions inside or near the superconducting magnet (Fig. 5.4 & 5.6). The pumping cell had a gas composition of $Xe/N_2/^4He$ at a pressure of 73/365/3210 torr (23 ^{0}C). Laser light had to be re-collimated for the different positions. The coupling of laser light to the windows of the pumping cell was optimized with considerable effort. However, there could still be variation between different positions. The polarizer was run in continuous flow mode at several different temperatures. The gas-flow rate was 0.22 l/min. All the flowing gas was transferred through Teflon tubing to a center glass cell which was enclosed by a Helmholtz coil for NMR signal measurements. The center cell was near the center of the 10120 gauss superconducting magnet (Position F, Fig. 5.4 & 5.6). A line-narrowed diode laser bar with a net output power of 21 watt was used at position A, E and I. For one of the test, because of space limitation, instead of line-narrowed diode laser, a17 watt fiber array packaged diode laser was used at position H. Position A was in a magnetic field of ~ 876 gauss that was fairly inhomogeneous, positions E and F were in a field of 10120 Gauss that was very homogeneous, position H was ~50 Gauss and very inhomogeneous, and position I was ~45 Gauss and very inhomogeneous (Fig. 5.6).

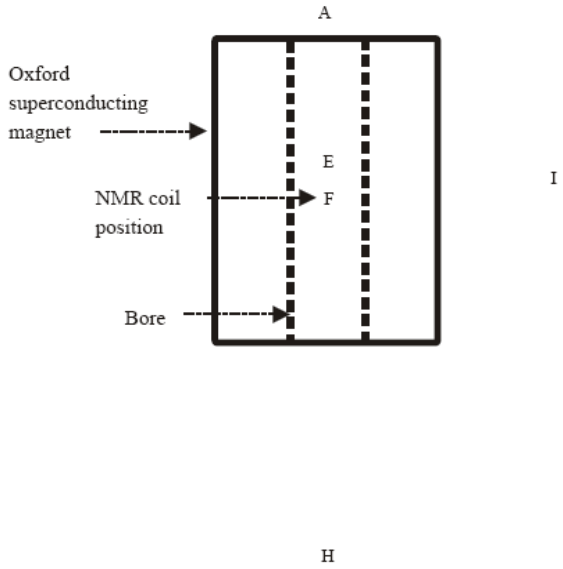

Fig. 5.4: Pumping cell and NMR coil position in continuous flow xenon experiment. The dashed line stands for the bore of the Oxford superconducting magnet. Distance and magnetic field values were also shown in fig 5.6. All the flowing gas from cells located in positions A, E, H & I were transferred to the cell located in position F which was enclosed by a Helmholtz coil for NMR measurement. Position I was ~127 cm lateral to the center and its field was ~45 gauss. Position H was ~225 cm backward to the center and its field was ~50 gauss.

5.2.3 Results and Discussion:

In Fig. 5.5, the NMR FFT amplitudes are plotted vs. temperature for each of positions A, E, I, and H.

Position A had higher signals than position E at every temperature tested. Surprisingly, position A was located outside of the magnet bore and its magnetic field was ~876 gauss and inhomogeneous, while position E was located at the most homogeneous place inside the magnet bore and its field was at 10120 Gauss. Our interpretation was that even at a cell gas composition of $Xe/N_2/^4He$ at a pressure of 73/365/3210 torr, there were still significant van der Waals interactions at ~876 Gauss. The high field of 10120 Gauss might have additionally quenched the van der Waals

process. The benefit of reduced xenon wall relaxation in high magnetic and homogeneous field could not compensate back the loss in spin-exchange efficiency.

Measurements were also made at two additional locations (I and H) in order to study the polarizer's performance at significantly lower magnetic field strengths. The magnetic field in these positions was quite inhomogeneous, and for practical reasons, the available laser power was lower than usual in position H. Nevertheless, we included these results for completeness. If nothing else, they showed that reasonable performance was still possible even in conditions that were far from ideal (Fig. 5.4, 5.5).

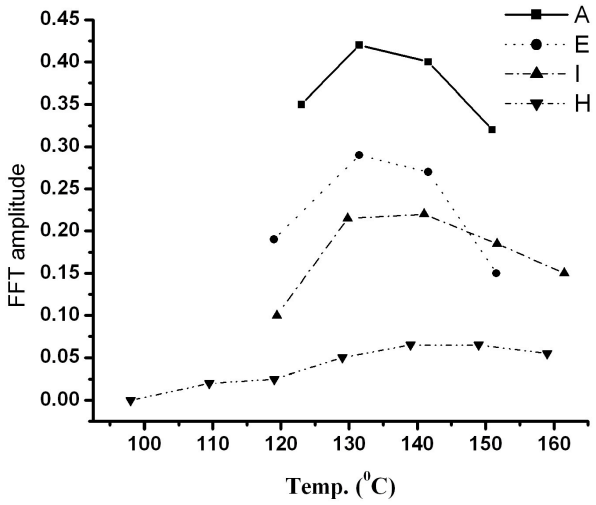

Fig. 5.5: Temperature scanning for continuous flow xenon experiment. Spin-exchange optical pumping was performed in cells positioned in and around the magnet at 4 different positions A, E, H, and I. At each position, experiment was run at several temperatures to determine the optimal operating point. Each flowing polarized xenon gas was transferred to a cell located in position F which was enclosed by a Helmholtz coil for NMR measurement. The NMR FFT amplitudes were plotted vs. temperature at each position. The lines connecting the data points are strictly to guide the eye. (Positions A, E, H, I and F were defined in Fig. 5.4) As shown, Position A had higher signals than position E at every tested temperature. Surprisingly, position A was located outside of magnet bore and its magnetic field was ~880 gauss and non-homogeneous, while position E was located at the most homogeneous place inside the magnet bore, its field was 10120 gauss.

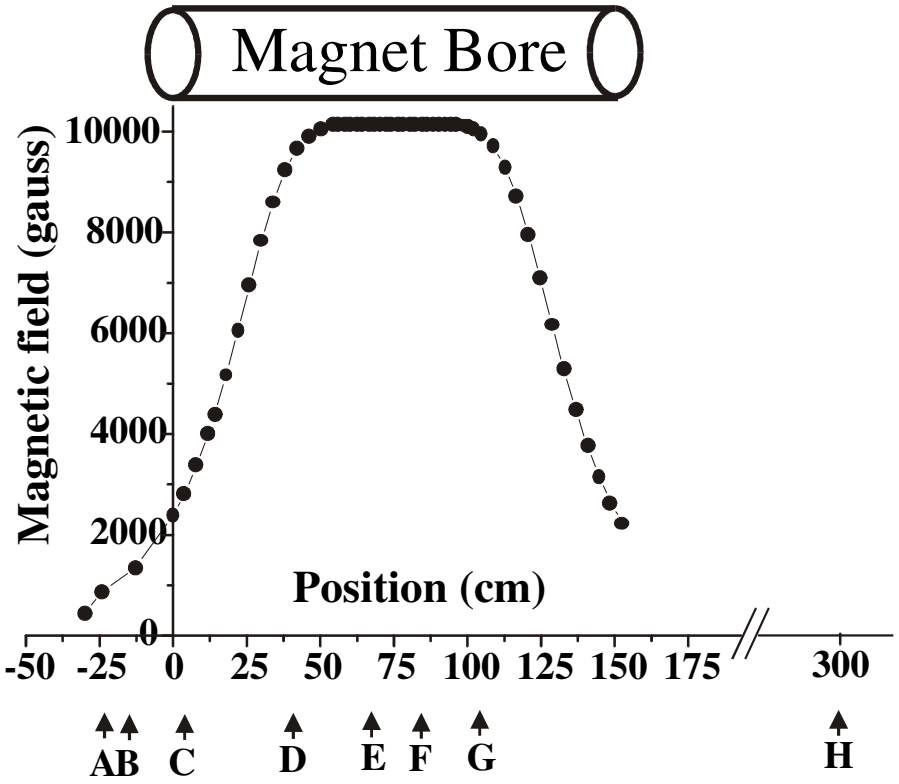

Fig. 5.6: Magnetic field mapping of Oxford superconducting magnet. The magnet bore spans from 0 cm to 152 cm. Letter A to H are positions of the pumping cells and accumulator in different xenon continuous flow and accumulation experiment.

5.3 Accumulation studies at different magnetic field values

5.3.1 Introduction

As mentioned earlier, the results from the flowing-gas studies described in the previous section came as something of a surprise. At high pressure, where we operate, it is not at all clear from the data in the literature that one should expect a significant difference in the spin-exchange rate between 10120 gauss at position A and 880 gauss at position E. Still our results indicated a significant difference. We thus undertook a test to confirm this observation.

5.3.2 Materials and methods of xenon accumulation experiment

The xenon pumping cell and accumulator were separated and placed at different locations for optical pumping and accumulation. Laser light had to be re-collimated for the different positions. The coupling of laser light to the windows of pumping cell was again optimized. However, there could still be variation between different positions. Polarized xenon gas mixture from the outlet of the pumping cell was transferred to the accumulator by the same Teflon tubing in each experiment. The accumulator was enclosed by a liquid nitrogen Dewar to freeze out xenon. The experiment was run at a flow rate of 0.16 liter/min, a cell temperature of 130 ^{0}C, and a total accumulation time of 52 minutes. Thawed-out xenon was sampled by a small bulb, which by virtue of the filling techniques was at 760 torr. The bulb was then put into a small solenoid NMR probe located in the magnet bore. Results from different locations were shown in Table 5.3. Position and field information were also presented in Fig. 5.6.

5.3.3 Results and discussion of accumulation experiment

Accumulation studies were performed as summarized in Table 5.3. Some effort was made to alternate back and forth between low and high magnetic field values to reduce systematic errors, and isolate the effect of magnetic field. For example, the cell condition might improve or deteriorate as time went on.

The most homogeneous field region of the magnet is from 80cm to 100 cm (positions F & G). The other positions have poor field homogeneity. For experiments under the same accumulator conditions(studies 2-6), pumping cell at position B(~1270 gauss) had a trend to gave higher polarization than position F with 10120 gauss and homogeneous field (studies 2, & 3 vs. studies 4 & 5 in Table 5.3).

Further experiments under the same accumulator condition, pumping cell at position B (~1270 gauss) had higher polarization than cell at position D (~9446 gauss)(studies 4 & 5 vs. study 6 in Table 5.3).

Tests done with the pumping cell at same position B (~1270 Gauss) but with xenon accumulated at a different position C (~2700 gauss with poor homogeneity) and position G (~9700 gauss with fairly good homogeneity) showed that the latter one gave 36% higher polarization (study 1 vs. studies 4 & 5 in Table 5.3) This result supports the benefit of one of our design principles, that the xenon should be polarized and accumulated within one reasonably homogeneous field to minimize losses.

Both xenon continuous flow (section 5.2) and accumulation (this section) experiments showed that spin-exchange pumping performed at low field, inhomogeneous position was even better than experiments done at high field and homogeneous region. If we operate the optical pumping at low and homogeneous field, then the result might be

even better. Because of the large fringe field of the superconducting magnet, we could not find a nearby ideal position to test on this. However, our speculation and discussion described in section 2.3 and section 5.1.2 were verified.

Table 5.3: Field effect on thawed-out xenon signal strength

Study number	Time sequence	Cell position, field (gauss), & homogeneity	Accumulator position, field (gauss), & homogeneity	Gas flow Liter/min	Signal Vp-p
1	20060801 11:33	B /~1270 poor	C /~2700 poor	0.16	2.20
2	20060803 15:34	F /10120 best	G /~9970 good	0.13 ~0.14	1.96
3	20060804 19:55	F /10120 best	G /~9970 good	0.16	2.90
4	200600806 21:33	B /~1270 poor	G /~9970 good	0.16	3.15
5	20060807 11:46	B /~1270 poor	G /~9970 good	0.16	2.95
6	20060807 14:36	D /~9446 poor	G /~9970 good	0.16	2.48

Note: Positions B, C, D, F and G are graphed in Fig. 5.6.

Chapter 6 Pumping cell and coating

6.1 Pumping cell

(Fig. 6.1, 6.2)

The pumping cell used in the MITI commercial polarizer which our group maintained regularly is a simple design of a cylinder with two windows on both sides for laser light passage. This type of cell is similar to that used by Driehuys et al. in 1996. An inlet and an outlet capillary were attached to the side-wall. A small bulb was included on the inlet capillary to be used as a rubidium "carburetor". The bulb was filled with rubidium to help saturate the incoming gas with rubidium vapor (Fig 6.1 A, 6.2 A). This type of cell had been used for a long time. It is cost-effective and easy to maintain. For the new xenon gas polarizer, it was thus natural to stick with this design. The first several pumping cells with which we worked, which we designate cell #1, and cell #2 were similar to the aforementioned cell. We were concerned, however, with the possibility that incoming gas might not be getting heated sufficiently quickly, resulting in Rb number densities that were less than what we intended (Chupp and Swanson 2001; Ruset, et al. 2006).

6.1.1 Modification of rubidium "carburetor"

In the design used in cell #1 and cell #2, the Rb "carburetor" bulb has the inlet and outlet capillaries arranged face to face, as is indicated in Fig. 6.2 The incoming gas passed through the bulb body without hindrance. In the new design, we extended the capillary into the bulb and made it curved to blow on the bulb wall. This created more turbulence and increased the exposure of gas to rubidium vapor. In cell #3, the extended capillary

was designed to be smaller in caliber to increase the gas flow rate when the gas entered into the bulb (Fig 6.2).

6.1.2 Heat-up loop

In the cell #1 design, the segment of inlet capillary inside of the oven is only ~2.5 cm. We were concerned that there might not be enough time for the gas to heat up before it entered the pumping chamber (Chupp and Swanson 2001). A control experiment was done to investigate this issue.

We happened to have a long capillary pumping cell, which was cell #1. A heating tape was wrapped round the inlet capillary to heat up the incoming gas. The system was run in continuous flow mode. The flow rate was 0. 15 liter/min and the pumping chamber was controlled to be ~119 ^{0}C. The Helmholtz coil that enclosed the pumping chamber was used to monitor the ^{129}Xe polarization using the pulse NMR measurements. When the heating tape was turned off, and the capillary temperature was measured at 45 ^{0}C, the NMR signal strength was 0.05. When the heating tape was turned on, and the capillary temperature was controlled to be ~100 ^{0}C, the NMR signal strength increased to 0.055 in one test and 0.07 in another test. Our interpretation was that heating the inlet capillary possibly helped to increase the xenon polarization, and was almost certainly not harmful.

We decided to modify our design by adding a loop of capillary on the input to the aforementioned Rb “carburetor”, as shown in Fig. 6.2. This series of cells were designated as loop cell. The gas mixture would thus have more time to heat up and theoretically would become better saturated with rubidium vapor as it passed through the Rb “carburetor”. The pumping cell could still be placed inside of the oven after adding the extra loop capillary, but it was a tight fit.

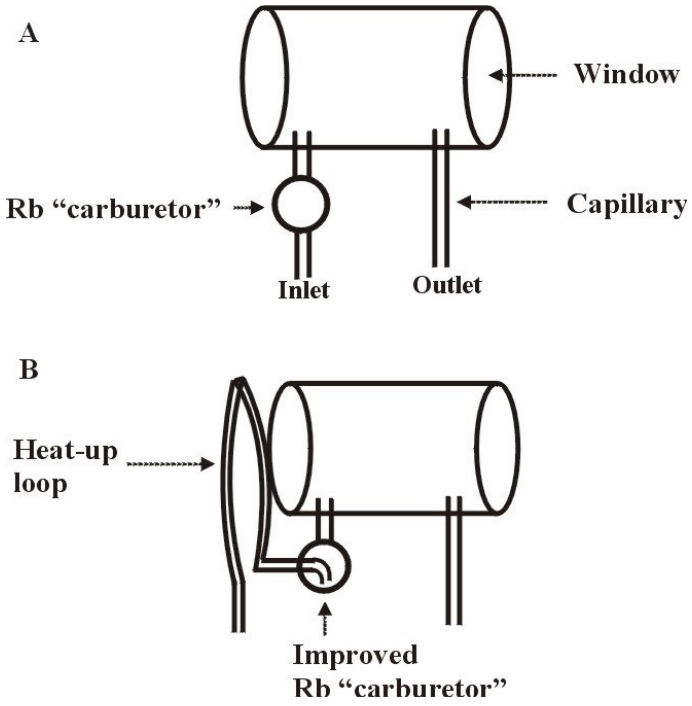

Fig 6.1 First pumping-cell design and its modification. A. Cell #1 design. The small bulb of the inlet capillary was filled with rubidium so that the incoming gas would be saturated with rubidium vapor. B. Modified pumping cell. A small capillary segment was added into the small bulb to dampen the gas flow and create turbulence and to increase rubidium vapor saturation. Furthermore, a new loop was added for heating up the incoming gas more thoroughly.

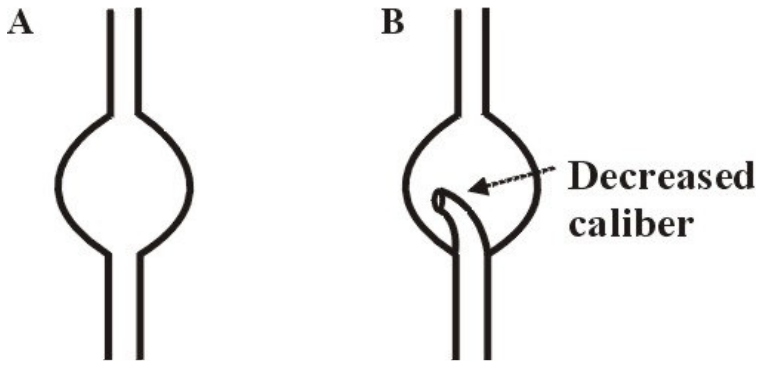

Fig 6.2 Modification of rubidium "carburetor". A. Original Rb "carburetor". Two capillaries were arranged end on. B. Modified version extended a smaller caliber capillary into the bulb. The orifice was directed to blow gas on the bulb wall. This increased the turbulence and exposure of the gas to the rubidium vapor.

6.2 Coatings

6.2.1 Introduction

It has long been established that wall coatings can reduce the wall-induced spin relaxation of ^{129}Xe nuclei in glass cells (Zeng et al. 1983). As discussed earlier, longer wall relaxation times contribute to higher polarization. While we tried several coating recipes that are described in the literature, we met with only limited success.

Many coatings methods are reported in the literature. Some report wall relaxation times of more than several hours (Breeze et al. 2000). It is important to note, however, that some of these studies were done on glass vessels under particularly favorable

conditions. It may be the case that our xenon cells were subjected to higher temperatures and more corrosive alkali-metal vapors than was the case for some of the other studies.

Most of the coating methods involve applying siliconization chemicals onto the cleaned glassware. These chemicals attach to the siloxyl groups (Si-OH) on the glass and its side chains react to form a hydrophobic blanket on the glass surface.

Sol-gel technology synthesizes glass from liquid solution at low temperature. A thin layer of aluminosilicate film coats the glass surface. Its homogeneity and purity should be better than standard glass making process. Chemicals used include tetraethyl orthosilicate (TEOS, $SiO_4(C_2H_5)_4$), water (H_2O), and ethanol (C_2H_5OH). The chemical process includes hydrolysis of alkoxide groups,

$$\text{-Si-OR} + \text{H-OH} \rightarrow \text{-Si-OH} + \text{ROH}$$

(where $R=C_2H_5$), and condensation to form siloxane bonds (-Si-O-Si-)

$$\text{-Si-OH} + \text{HO-Si-} \rightarrow \text{-Si-O-Si-} + H_2O$$

$$\text{-Si-OH} + \text{RO-Si-} \rightarrow \text{-Si-O-Si-} + \text{ROH}$$

This forms an amorphous silica network with a wet gel appearance. Aluminum nitrate nonahydrate ($Al(NO_3)_3{\cdot}9H2O$) can added to form an aluminosilicate ($Al_2O_3{\cdot}SiO_2$) network(Tobias et al. 2002).

With limited resources and time, we could not do large numbers of control experiments on different coatings. However, we tried several coatings that we thought would be promising and measured the intrinsic wall relaxation times, as well as other properties related to spin-exchange optical pumping using the methodology described in Chapter 5.

Firstly, both the accumulator and the gas sampling bulb were coated with either octadecyltrichlorosilane(OTS) or Surfasil. Secondly, the pumping cells were either left uncoated, or coated with Sol-gel, DryFilm, SC-77, or Surfasil.

6.2.2 Glassware cleaning

We give below the glassware cleaning procedure we used which followed the recipe of the Walsworth group (Walsworth et al. group manual).

1. Firstly use warm Citronox (2% solution) and shake the glassware for a few minutes. Use deionized water to rinse completely several times.

2. Prepare Piranha solution (volume ratio of sulfuric acid to hydrogen peroxide(30% strength) equals 7 to 3). Rinse the glassware and soak it for one hour to 12 hours. Use deionized water to rinse completely several times.

3. For drying, use methanol to rinse several times. Bake glassware in the oven at ~100 ^{0}C for one to 2 hours; could also blow dry the cell with nitrogen or helium gas, this will leave some residual water on the surface for reaction with silanes.

6.2.3 Coating methods:

1. OTS (Fig. 6.3) (Walsworth et al. group manual.)

1) After cleaning, the cell was wetted again using distilled water and then air dried by nitrogen gas.

2) Prepare an organic solution of 1 part chloroform and 4 parts hexanes, by volume under hood.

3) Add octadecyltrichlorosilane 0.8 ml per 1 L of chloroform/hexanes solution.

4) Soak glass in solution for 5 minutes.

5) Dip dry in air for 5 minutes.

6) Rinse the glassware with chloroform 3 times under hood.

7) Use turbomolecular pump to bake dry the glassware at 200 ^{0}C for 24 hours.

2. Sol-Gel (Tobias et al. 2002)

1) Add 11.32 gram of aluminum nitrate nonahydrate ($Al(NO_3)_3.9H2O$) into 5 ml deionized water and 70 ml ethanol. Stir in a flask with a magnetic stirrer for one day.

2) Add 10.3 ml tetraethyl orthosilicate ($Si(OC_2H_5)_4$) into the solution. Stir for 2-5 days.

3) Add ethanol to the solution for 7:1 dilution before use.

4) Soak the cell for 3 hours.

5) Drip dry for 3 hours.

6) Bake the cell at 60 ^{0}C for 9 hours, then sinter it at 550 ^{0}C for 2 hours.

7) Each cell was coated with the above procedure for twice.

8) Vacuum pump the cell at 250 ^{0}C for 2-3 days.

9) Chase rubidium into the string, flame bake and then chase rubidium into the cell.

3. "Dryfilm" (Fig. 6.3)(Swenson and Anderson 1988)

1) Mix dimethydichlorosilane with deionized water in 2:1 volume ratio into flask.

2) Expose the cell to the vapor for 2-3 minutes.

3) Bake the cell in 200 ^{0}C for 3 hours.

4) Pre-pump with roughing pump through liquid nitrogen trap to condense the vapor, while heating the cell to ~220 ^{0}C.

5) Vacuum pumping and baking with a vacuum pressure of 10^{-8} torr and oven temperature of 250 ^{0}C.

6) Rubidium was chased into the cell through the pull-off stump.

4. SC-77 (Fig. 6.3)(Fedchak et al. 1997)

1) Mix dimethyldichlorosilane (DMDCS) with methoxytrimethylsilane (MTCS) in 2:1 volume ratio, and swirl well.

2) Add deionized water to the DMDCS & MTCS solution in a 1:6 volume ratio. This prepared a 65% DMDCS, 35% MTCS solution.

3) Expose the cell to the vapor created by the above solution for 10 minutes.

4) Expose cell for 5 minutes to a solution of 95 ml methanol/ 5 ml deionized water with some acetic acid and 5% MTCS.

5) Pour out and rinse with copious amounts of methanol and deionzed water.

6) Attach cell to a string and vacuum pump at room temperature for about 24 hours and then at 92 ^{0}C for about 60+ hours.,

7) Chase rubidium into the string. Avoid having it enter the cell. Keep the cell temperature less than 100 ^{0}C.

8) Warm the string and the cell to about 50-70 ^{0}C and let the Rb roll into the cell.

5. Surfasil (Fig. 6.3) (Breeze et al.2000)

1) Prepare 15% solution of SurfaSil/hexane (15ml of SurfaSil into 100 ml of hexane).

2) Soak the cell for about 1 hour.

3) Rinse the cell with hexane and then methanol.

4) Blow dry the cell with nitrogen gas.

5) Bake the cell at 90 ^{0}C in air for about 2 hours.

6) Vacuum pump the cell for 48 hours at room temperature.

7) Chase rubidium into the string. Avoid having it enter the cell. Keep the cell temperature less than 100 ^{0}C.

8) Warm the string and the cell to about 50-70 ^{0}C and let the Rb roll into the cell.

6.2.4 Results and discussion

(Table 6.1)

Interestingly, the maximal static xenon polarization (87.5%) and thawed-out polarization (17.9%), was achieved in an uncoated cell, #2. Its wall relaxation time constant was 712 seconds. Unfortunately, the cell's performance deteriorated after refurbishing. Maximal static polarization reduced to 22%, while thawed-out polarization decreased to 14.5%. Similar findings were noted in other pumping cells produced for the MITI polarizer (Tobias 2006). We hope to obtain a better coating method for our application.

One Sol-gel coated cell achieved a static polarization of 71%, and a wall relaxation time constant of 287 seconds. This cell was stored for almost 10 months before it was used, however the performance was still good. Rubidium deposition on windows was a problem with cells coated with Sol-gel technology. Rubidium deposition on the front window blocks laser light, while light reflection from back window tends to depolarize rubidium spins.

One SC-77 coated cell achieved a static polarization of 65%, a thawed-out polarization of 12.1% and a wall relaxation time constant of 1610 seconds. This cell showed interesting behavior that its performance improved after usage. Both static polarization and wall relaxation time constant increased. This might be a kind of progressive curing from oven baking or rubidium deposition. This cell was kept below 100 ^{0}C during preparation. It was also kept below ~120 ^{0}C during optical pumping. This was to preserve the integrity of the SC-77 coatings.

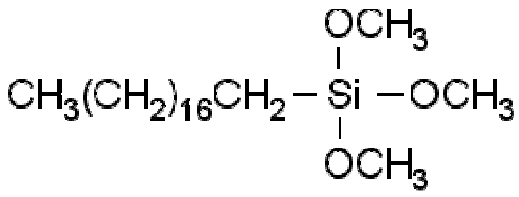

octadecyltrimethoxysilane (OTS)

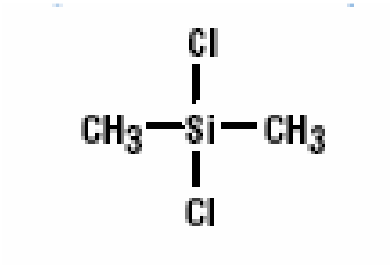

dimethyldichlorosilane (DMDCS)

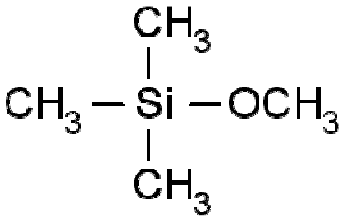

methoxytrimethylsilane (MTCS)

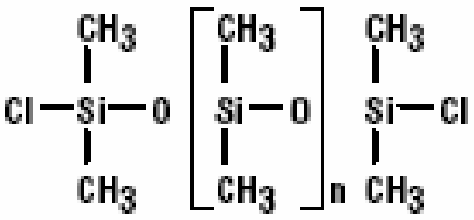

dichlorooctamethyltetrasiloxane

Fig. 6.3 Chemical structure of octadecyltrimethoxysilane (OTS), dimethyldichlorosilane (DMDCS), methoxytrimethylsilane (MTCS) and dichlorooctamethyltetrasiloxane (Surfasil). (Technical data from ^{R}Pierce and ^{R}SigmaAldrich).

The "Dryfilm" coated cell was subject to 250 ^{0}C baking during preparation. Its performance was not good. One of the problems of silane coatings is their sensitivity to high temperatures under certain conditions.

It was suggested that Surfasil coating should not be subject to more than 100-120 ^{0}C. Our Surfasil coated cell was intentionally kept below 95 ^{0}C during preparation. It was also kept below ~120 ^{0}C while optical pumping. It achieved static polarization of 50% and thawed-out polarization of 6%. The performance was generally inferior to SC-77

coated cell (Table 6.1). This was consistent with the commercial advertisement that DMDCS (one chemical of SC-77 coatings) coating was more temperature-resistant than Surfasil coating (Technical data from ^{R}Pierce). SC-77 may be a promising coating method since our pumping cell is operated at more than 100 ^{0}C.

Table 6.1 List of cell coatings and performance.

Cell name	Coating	Baking temperature (^{0}C)	wall relaxation time(second)	static[a] polarization maximal (%)	% of xenon gas mixture used
#1	Sol-gel	~250	287	71	2
#1	refurbished	~250	806	26	2
#2	uncoated	~250	714	87	2
#2	refurbished	~250	422	22	1
#3	Dryfilm (DMCS)	~250	>483[b]	14	1
loop #1[c]	SC-77	<95	330/1610/ >646[b]	8/65/38	1/1/2
loop #2	uncoated	~250	461	38	1
loop #3	Surfasil	<95	>1070[b]	50	1

a: static means closed cell spin-exchange optical pumping operation.
b: ">" means that when using spin-experiment methodology as described in Chap. 5, the linear fitting went to negative wall relaxation time. The interpretation was that the cell coatings had interaction with rubidium and thus affected rubidium vapor density. Rubidium density was lower at low temperature. Apparent spin up time constant at lowest temperature was listed in the table for reference.
c: Wall relaxation measurements were performed for 3 times in loop #1 cell.

Chapter 7 Optimization and application

7.1 Optimization

To obtain optimal parameters for operating the polarizer, we undertook various static (closed cell) optical pumping, continuous flow and accumulation experiments. Xenon gas concentration, pressure, flow rate and temperature were varied to determine their effects on final polarization.

7.1.1 Static spin-exchange optical pumping

The two glass valves of the pumping cell were closed during static or non-flowing optical pumping. A series of spin exchange optical pumping measurements were performed with 1% and 2% xenon gas mixtures at different gas pressures and different temperatures to investigate the optimal operating parameters for our polarizer. The general methods of the spin-up experiments employed were described in Chapter 5.

As shown in Fig. 7.1, at 1% xenon gas concentration, low pressure conditions yielded higher static polarization. We know that pressure broadening effects decrease as pressure goes down. This implies that our line narrowed laser spectrum was still within the narrower absorption trough at the low pressure of 2204 torr. Furthermore, increasing laser power density should increase our polarization more. Fig. 7.2 shows similar results for 2% xenon gas mixture.

In Fig. 7.3, the data for 1% and 2% xenon gas mixtures are compared to each other for each of the two pressures of 2204 and ~3648 torr. At both pressures, higher polarizations were obtained with 1% xenon mixtures, a trend that indicates that the

optical pumping rate was not sufficient to overwhelm the electronic spin relaxation due to the xenon.

We also noticed that the maximal polarization occurred at 80 – 90 ^{0}C oven temperature. It was noticed that the cell surface temperature was usually 20-30 ^{0}C higher than the oven temperature.

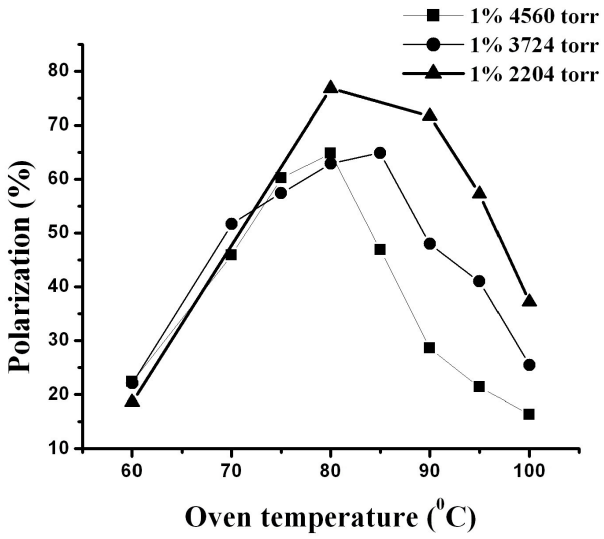

Fig. 7.1 Static optical pumping of 1% xenon gas mixture at 2204, 3724, and 4560 torr pressure. Static optical pumping was performed and maximal xenon polarization was measured at different temperatures and different pressures. Lower gas pressures had higher polarizations.

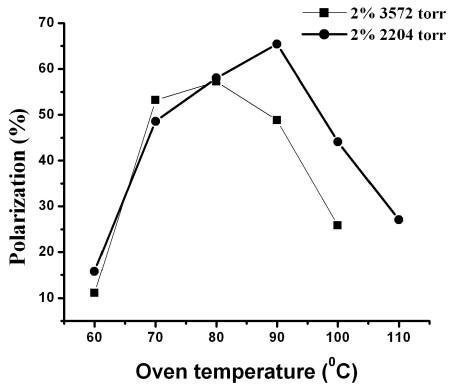

Fig. 7.2 Static optical pumping of 2% xenon gas mixture at 2204, and 3572 torr pressure. Static optical pumping was performed and maximal xenon polarization was measured at different temperature and different pressure. Lower gas pressure had higher polarization.

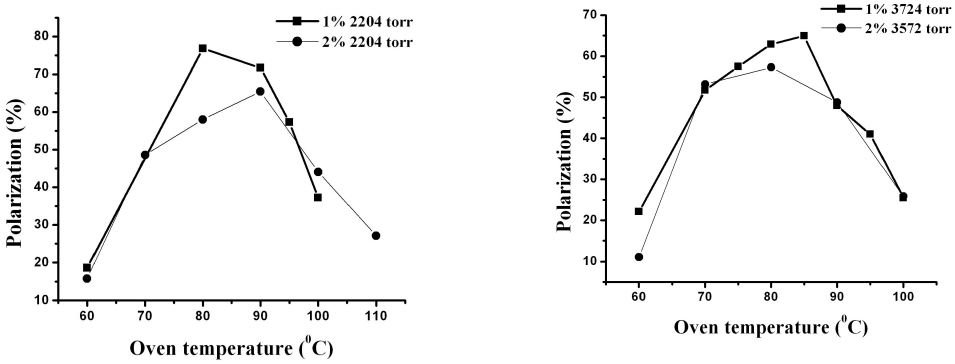

Fig. 7.3 Comparison of 1% and 2% xenon gas mixture polarization yield in static optical pumping at similar pressures. As shown in the hand side graph, 1% xenon gas mixture had higher polarization yield than 2% gas at 2204 torr. Similar findings were also shown in the right-hand graph at 3572-3724 torr.

7.1.2 xenon continuous flowing/temperature scanning experiment

The xenon gas polarizer was put in a continuous-flow mode without accumulating the xenon gas. A Helmholtz coil enclosing the pumping cell inside the oven was used to measure the NMR signal. This signal was assumed to reflect the total average polarization of the whole pumping cell while flowing xenon gas. The outlet gas polarization may be higher than the average value. In addition to 2 line-narrowed lasers with a total power of ~32 watt, one Coherent fiber array package diode laser of ~17 watt was used, though this laser's spectrum was very broad.

As shown in Fig. 7.4, 2% xenon gas mixture at 3572 torr was flowing at 0.35, 0.16 and 0.10 liter/min. Compatible with static pumping, maximal polarization occurred near 90 ^{0}C oven temperature. Cell surface temperatures were probably 20-30 ^{0}C higher than the oven temperature. Lower flow rates yielded higher polarizations.

Similarly, shown in Fig. 7.5, 1% xenon gas mixture at 3572 torr was flowing at 0.2 and 0.10 liter/min. Lower flow rate also yielded higher polarization.

Comparing Fig. 7.4 and Fig. 7.5, under the same conditions of 0.1 L/min flow rate, ~90 ^{0}C and 3572 torr, 1% xenon gas yielded ~32% polarization, while 2% xenon gas was ~23%.

Shown in Fig. 7.6 was 1% xenon gas mixture at different pressures of 2280, 3572, 4104, and 4560 torr with a continuous flow rate of 0.2 liter/min. Gas of 3572 torr yielded the highest polarization. For this experiment, there were two main factors affecting the polarization. The first was the gas transit time through the pumping cell. For a given flow rate at standard condition, a high pressure cell had slower flow and thus had more time to

become polarized. The second factor was that with low pressures higher rubidium polarizations resulted as discussed in section 7.1.1. While the precise weighting between these two competing factors in determining the final polarization was unknown; however, setting the cell pressure to 3572 torr yielded optimal performance.

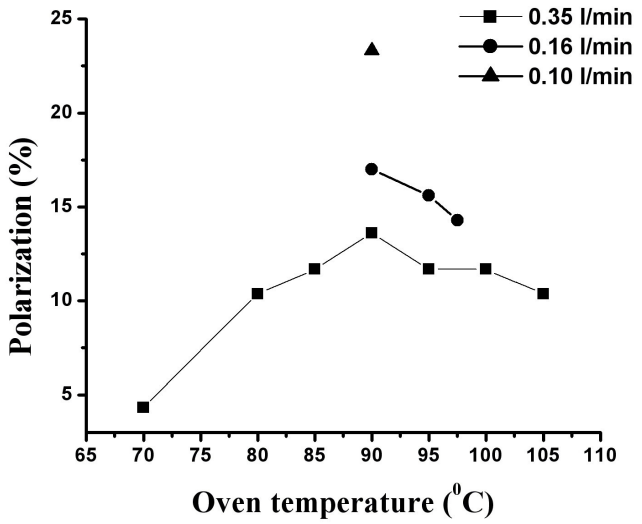

Fig. 7.4 2% xenon gas continuous flow and temperature scanning study (experiment time and file name: 20060518). 2% xenon gas mixture at 3572 torr was flowing at 0.35, 0.16 and 0.10 liter/min. The polarization was measured by a Helmholtz coil enclosing the pumping cell inside the oven. Compatible with static pumping, maximal polarization occurred near 90 ^{0}C oven temperature. Cell surface temperature might be 20-30 ^{0}C higher than oven temperature. Lower flow rate yielded higher polarization.

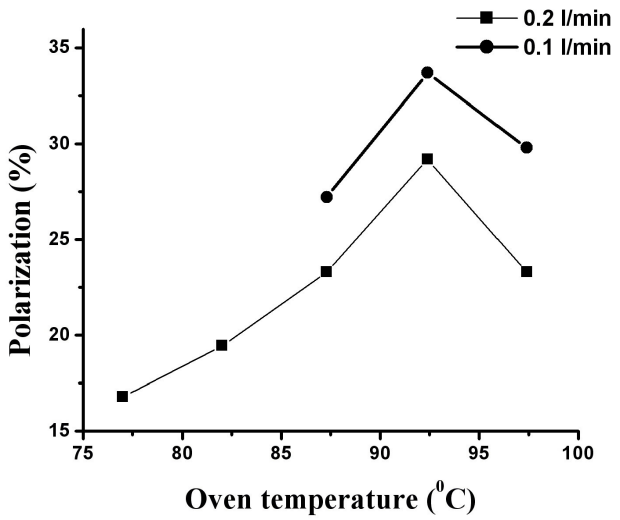

Fig. 7.5 1% xenon gas continuous flow and temperature scanning study (20060520). 1% xenon gas mixture at 3572 torr was flowing at 0.2 and 0.10 liter/min. Compatible with static pumping, maximal polarization occurred near 90 ^{0}C oven temperature. Cell surface temperature might be 20-30 ^{0}C higher than oven temperature. Lower flow rate yielded higher polarization.

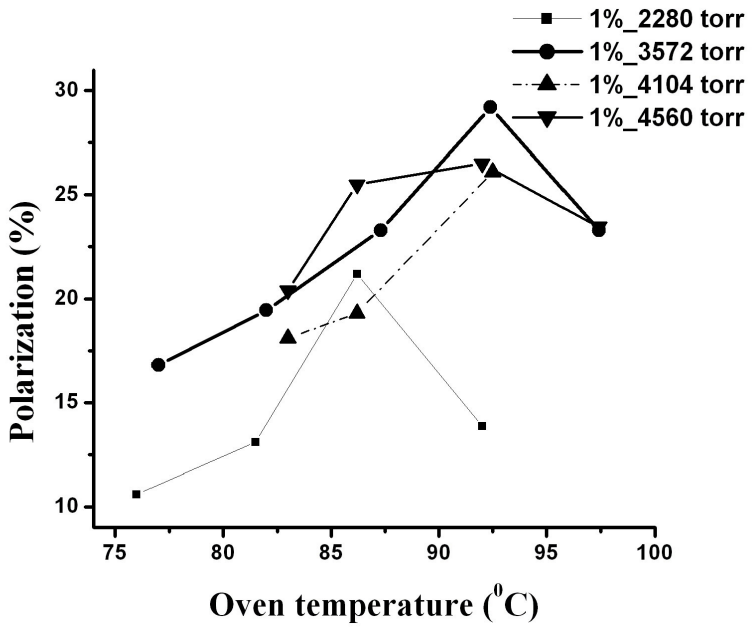

Fig. 7.6 1% xenon gas continuous flow and temperature scanning study (20060520). 1% xenon gas mixture at different pressures of 2280, 3572, 4104 and 4560 torr, with a flow rate of 0.20 liter/min. 3572 torr yielded the highest polarization.

7.1.3 Xenon accumulation experiment.

The xenon gas polarizer in accumulation mode needed more consideration than in static operation or during a continuous flow experiment. During accumulation, the polarized xenon gas went through a glass accumulator which was enclosed by a liquid nitrogen bath. Helium-4 gas and nitrogen would pass through, while xenon would be frozen in the accumulator. The solid xenon relaxation time constant inside the accumulator was around 150 minutes at 5000-6000 gauss permanent magnet field condition as in the current MITI polarizer. It could be longer at our superconducting magnet which was at 10120 gauss with more homogeneous field. The polarization of xenon P_{Xe}, after an accumulation time T_{total}, can be expressed as:

$$P_{Xe}(T_{total}) = \frac{P_{Xe}(0)T_1\left[1 - e^{-\frac{T_{total}}{T_1}}\right]}{T_{total}} \qquad \textbf{(7.1)}$$

where $P_{Xe}(0)$ is xenon polarization before being frozen; T_1 is the solid xenon relaxation time; and T_{total} is the total accumulation time (Driehuys et al. 1996). While the gas mixture flow rate does not show up in this equation directly, it has profound impact on the final polarization by affecting $P_{Xe}(0)$ and T_{total}. As presented in Fig. 7.5, low flow rates led to higher polarization in continuous flow mode, and $P_{Xe}(0)$ became higher. On the other hand, T_{total} was also a function of flow rate. If we want to accumulate a certain amount of xenon, low flow rates increase the required accumulation time T_{total} and this can decrease the final polarization.

We described the problems of temperature gradient across the xenon ice in the accumulator in section 2.3. The true T_1 should actually be an integral of different T_1's across the xenon ice, instead of T_1 at a temperature of 77 K (the liquid nitrogen bath temperature). Therefore, the final polarization should be less than equation 7.1 predicts.

Many xenon accumulation trials were done in the past several months. Several of the better results are presented here. We noticed that running the system at low flow rate usually yielded higher polarization. Since our system was inside a superconducting magnet, longer accumulation time was acceptable. 1% xenon gas mixture only increased polarization a little more than 2% xenon gas mixture. However, using 1% gas doubled the accumulation time. Practically, 2% xenon gas is a better choice for our system. The details of experimental parameters and results are listed in Table 7.1.

At the time of this writing, the best thawed-out xenon polarization was 17.9%. It was achieved in a fresh uncoated pumping cell, using 1% xenon gas mixture, a flow rate of 0.12 L/min, and accumulation time of 106 minute. The signals and parameters for calculating xenon polarization for this experiment were presented in Table 7.2 and Fig. 7.7.

Table 7.1 Xenon Accumulation experiments parameters and results[a]

Date 2006	Cell name	% of xenon gas mixture	Flow rate (L/min)	Temperature (^{0}C)	Accumulation time (min)	Thawed-out Xenon volume (ml)	Thawed-out Xenon polarization (%)
0504	#2	1	0.4	85 (oven)	50	200	15.8
0519	#2	2	0.11	88 (oven)	92	202	16.7
0520	#2	1	0.12	95 (oven)	106	127	17.9
0801	Refurbished #2	2	0.16	128	48	154	10.4[b]
0806	Refurbished #2	2	0.16	128	50	160	14.5
0807	Refurbished #2	2	0.16	128	50	160	13.6
0925	Loop #1	2	0.35	117	35	245	8.6
0929	Loop #1	2	0.27	120	46	248	11.2
1011	Loop #1	1	0.28	120	48	134	10.8
1013	Loop #1	1	0.1	125	~100	~100	12.1
1108	Loop #1	1	0.52	125	64	333	10.2[c]
1110	Loop#1	1	0.50	125	103	515	9.0[c]

a: all cell pressure at ~3648 torr (room temperature).
b: accumulator located at the inhomogeneous, 2000 gauss field of the open end of the magnet.
c:using different ¼ waveplate.

Table 7.2 Polarimetry parameters for the experiment of maximal thawed-out xenon polarization[a] (experiment time and file name: 20060520181007)

	Enriched xenon phantom	Thawed-out xenon in the bulb (760 torr, 20 ^{0}C)
Relative amplification fold	10000	20
^{129}Xe density	6.299E-4 mole/ml	1.0998E-5 mole/ml
^{129}Xe abundance (%)	86.2	26.44
Cell gas composition	83.33% xenon	100% xenon
Signal strength (volt) at ~600 μsec point	0.23[b]	1.47
Polarization	9.77 x 10^{-7} thermal equilibrium (20 ^{0}C)	**Result: 17.9%**

a: using cell #2
b: using xenon phantom calibration at ~70 cm position (Section 3.4.3)

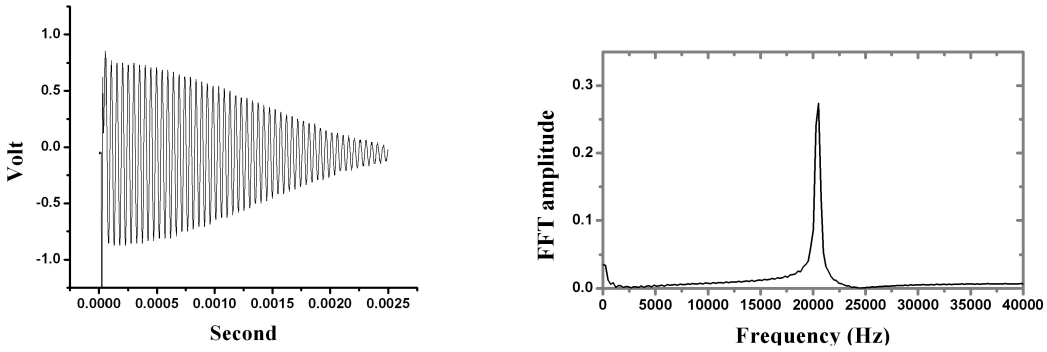

Fig. 7.7 NMR signal of thawed-out xenon gas (experiment time and fiel name: 20060520181007). Shown in left-hand graph was the signal tracings. Voltage peak-to-peak near ~600 μsec region was measured for polarimetry (Table 7.2). Because of magnet space limit, the solenoid coil was not put in the most homogeneous place, therefore, the T_2^* was short. Right-hand graph showed the amplitude of Fast Fourier Transform. The polarization was 17.9%, (natural abundance).

7.2 Application

The new xenon gas polarizer was developed and built in a laboratory space inside the radiology department of the University of Virginia (UVA). At the late stage of development, we began to collaborate with researchers of Center for In-Vivo Hyperpolarized Gas MR Imaging of UVA. The polarized xenon gas was applied to either a plastic bag or rabbit for magnetic resonance studies.

7.2.1 Magnetic resonance imaging (MRI) preliminary

Space localization

To go one huge step from NMR to MRI, the major difference is space localization capability. In addition to the main holding field, gradient fields were applied in X, Y, and Z axes by saddle coils for three dimensional localization. The Z axis gradient was usually used for slice selection. Further two dimensional localization on the selected slice relies upon phase encoding or frequency encoding on either the X axis or the Y axis.

Fourier transformation and k-space (Nishimura, 1996)

For each run of RF pulse, every pixel on the selected slice is subject to specific gradient manipulation. The net signal from the entire sample s(t) (all those pixels in the selected slice) can be described as:

$$s(t) = \int_x \int_y m(x, y) e^{-i2\pi[k_x(t)x + k_y(t)y]} dxdy \qquad (7.2)$$

where m(x,y) is the small groups of spins on each pixel(x,y), and

$$k_x(t) = \frac{\gamma}{2\pi} \int_0^t G_x(\tau) d\tau \qquad (7.3)$$

$$k_y(t) = \frac{\gamma}{2\pi}\int_0^t G_y(\tau)d\tau \qquad (7.4)$$

G_x is the gradient applied along the X axis, and G_y is the gradient applied along the Y axis. The spatial frequency k_x and k_y are two variables of k space. To reconstruct the pixel magnetization, the gradient trajectories must cover the whole k space. After collecting all signals, a two dimensional Fourier transformation will regenerate m(x,y), which is the magnetization image in which we are interested.

Hyperpolarized gas imaging consideration

Spin-echo or gradient-echo pulse sequences are two conventional methods to obtain images. Spin-echo methods need one 90^0 pulse and later another 180^0 pulse for echo generation, while gradient echo uses bi-directional gradients to de-phase and re-phase spins. Furthermore, small flip angles are allowed in the gradient-echo method. Since the laser-pumped polarization of polarized xenon gas is non-recoverable, gradient-echo sequences are preferred over spin-echo sequences and are widely used in hyperpolarized gas imaging (Fig. 7.8).

7.2.2 Xenon gas diffusion coefficient study

The respiratory tract includes the trachea, the bronchus, the bronchioles, and the alveolar sacs. Pathology like emphysema or bronchial asthma will cause air trapping in some distal respiratory tract. Noble gas diffusion studies for obstructive lung disease have been developed for years. Local xenon gas diffusion coefficients may reflect the nearby alveolar or acinar space dimensions. It has been shown to be useful in the imaging of the regional extent of chronic obstructive pulmonary disease (Salerno 2002).

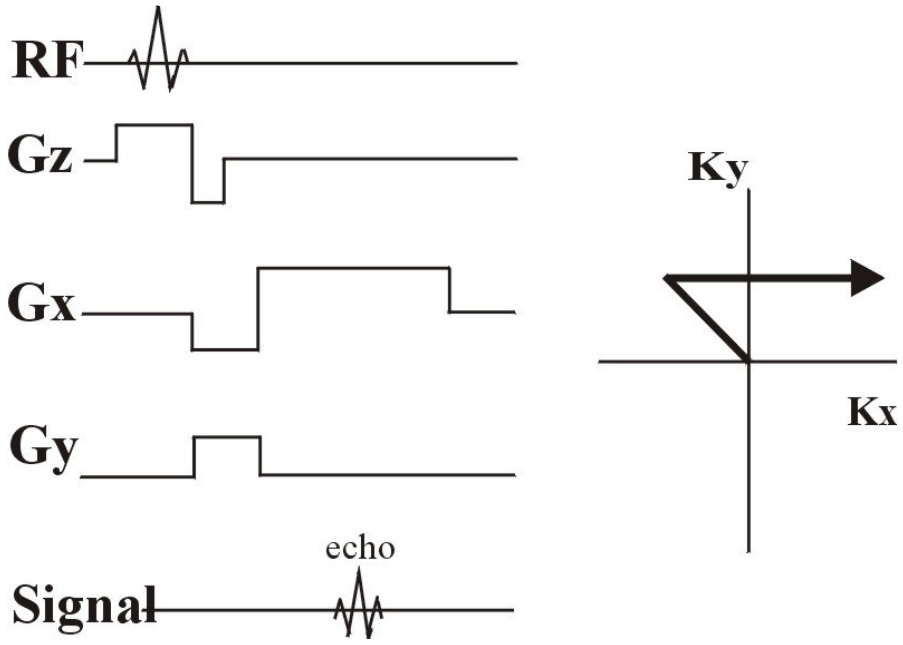

Fig. 7.8 Gradient echo imaging. Left) As a slice selective gradient is applied to the Z axis, a small or variable flip angle RF pulse is radiated. While a phase encoding gradient is applied to the Y axis, a bi-directional gradient is applied to X axis. On the signal tracings, notice the timing of echo generation. It happens when accumulated G_x gradient strength reverts to zero. Right) The time integrals of G_x, and G_y in k-space. Notice the initial negative direction in k_x axis and then go forward in the positive direction (equation 7.2, 7.3 & 7.4) (Nishimura 1996).

Historically, diffusion sensitive bipolar gradient methods have been applied in MRI to study xenon diffusion coefficients. Typically, bipolar gradient is applied with a specific strength, duration and interval. As the gas diffusion process proceeds, diffusing spins will not re-phase completely compared to non-diffusing spins (Fig. 7.9). Diffusion coefficient can thus be calculated from the signals (Mair et al.1998).

In the first preliminary studies we performed using gas from the new xenon polarizer, a bag of 9.4% polarized xenon gas was given to Dr. Wilson Miller and his student Michael Carl. The gas was scanned by a Siemens Sonata Scanner. The measured

T_1 lifetime in the bag was 1.7 hours. The measured xenon diffusion coefficient was 0.045 cm^2/sec, which was close to the expected free diffusion coefficient of 0.06 cm^2/sec.

7.2.3 Rabbit lung MRI imaging

In collaboration with Dr. Jaime F.Mata, we supplied the polarized xenon gas for lung-space imaging of several healthy rabbits. In one experiment, the polarization was first measured as 11.2 % (natural abundance), by our NMR apparatus (Fig. 7.10). The calibration at ~84 cm location was used in this calculation (Section 3.4.3). The Siemens Sonata scanner was subsequently used to make MR images. Three of the resulting coronal sections of anterior, middle and posterior rabbit lung are shown in Fig. 7.11. The imaging parameters were TR: 7.5 msec, TE: 3.04 msec, pixel resolution: $2.2 \times 2.2 \times 22$ mm^3, and pixel number: 128×64.

More than ten sets of imaging experiments were performed during a 6 week period. Some of the experiments are listed on the last 6 rows of Table 7.1. Included were runs in which we supplied 500 ml of 9.0% polarized gas. We note that we are currently optimized for somewhat smaller quantities. Also, some of the runs occurred while the MITI polarizer was used to produce polarized ^{3}He, thus facilitating direct comparisons of ^{129}Xe imaging with ^{3}He imaging.

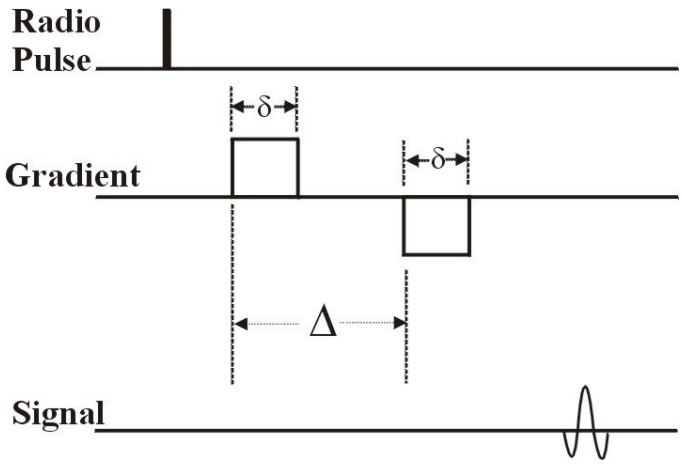

Fig. 7.9 Diffusion-sensitive bipolar gradient. A RF pulse firstly flipped the spins to the horizontal plane. A bipolar gradient was applied with specific strength, duration δ and interval Δ. As the gas diffusion process proceeded, diffusing spins would not re-phase completely compared to non-diffusing spins(Mair et al. 1998).

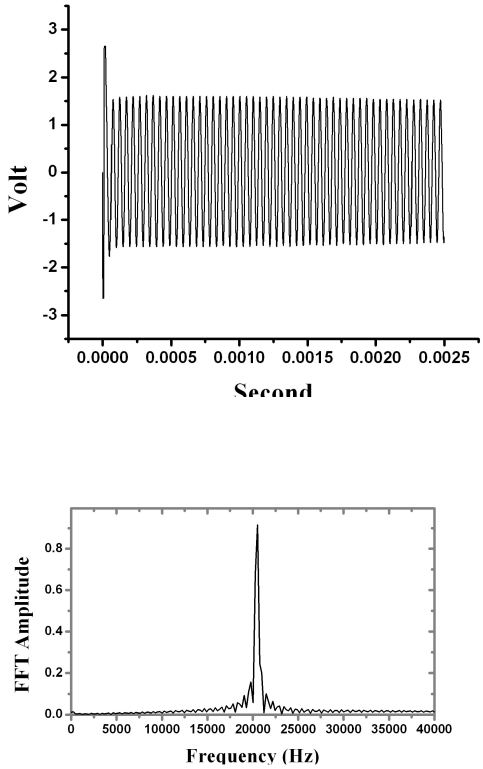

Fig. 7.10 NMR signal of polarized xenon gas applied for MRI rabbit lung imaging in Fig. 7.10. Shown in the upper graph was the time domain tracings, while the lower graph was the amplitude of Fast Fourier Transform. Measured polarization was 11.2%, natural abundance.

A

B

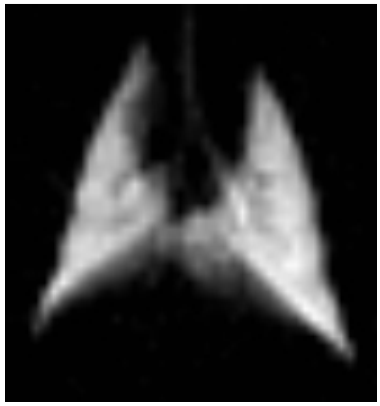

C

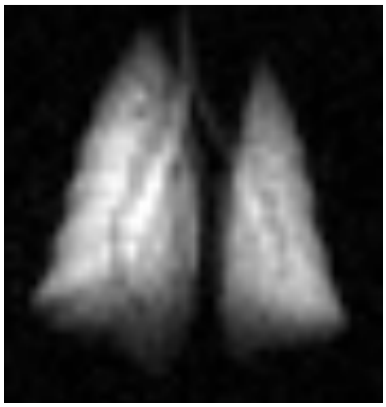

Fig.7.11 MRI lung imaging of rabbit. Polarized xenon gas was sent to image rabbit lung with a Siemens Sonata Scanner. The imaging parameters were TR: 7.5 msec, TE: 3.04 msec, pixel resolution: 2.2 X 2.2 X 22 mm^3, and pixel number: 128 X 64. Coronal sections of A) anterior thorax, B) middle thorax, and C) posterior thorax were presented. The polarization was 11.2%, natural abundance, measured by our custom-built and calibrated NMR apparatus, as shown in Fig. 7.9 (Image courtesy of Dr. Jaime F. Mata, Radiology, University of Virginia.)

Chapter 8 Conclusion

In this thesis I have described the results of studies that were undertaken during the last three to four years aimed at the development of a system for producing polarized ^{129}Xe with increased performance over what had previously been available. We went on to develop and construct a new xenon polarizer inside and around a superconducting magnet and have studied a variety of parameters on the spin-exchange optical pumping process. As a result of our efforts, we have increased the level of ^{129}Xe polarization over what was available previously using the MITI prototype polarizer. Furthermore, our results provide guidance for the construction of an economical high-performance polarizer that would be valuable to the noble-gas imaging community as a whole.

8.1 Summary of results and the contribution to the field of xenon polarization

An important outcome of this work was the demonstration of the practical advantage of using line-narrowed high-power diode laser arrays as an economical solution to improve the polarizer performance. Using external-cavity line narrowing technology, we narrowed the full-width at half-maximum of the diode laser spectrum from 2.5 nm to 0.17 nm (Fig. 4.5) which was consistent with expectations from the literature (Chann et al. 2000). We further devised a novel orthogonal geometry for orienting the axes of two diode-laser arrays to increase the homogeneity and power of the laser beam (Fig. 4.8). Optical pumping experiments showed an increase of ^{129}Xe polarization associated with the orthogonal geometry which verified the efficacy of this new laser configuration (Fig.

4.9). In comparing our results with those from an un-narrowed diode laser system (which we had previously installed in the MITI prototype system), we found significantly increased performance despite having roughly one-third to one-half the total laser power.

One of the surprises to come out of this research was that we are still starved for laser power despite coupling roughly 35 watts into the cell with a line-width that is approximately ten times narrower than previously. Evidence supporting this conclusion emerged consistently from many different studies. A good example are the data presented in Fig. 4.10 in which a signal proportional to polarization (FFT signal) is shown as a function of oven temperature for three configurations; diode laser #1 alone, diode laser #2 alone and both lasers together. If the laser power had been sufficient, there should have been much less of a difference between using one laser alone or two lasers together. Further evidence supporting the need for more laser power comes from the comparison of the "static" polarization tests illustrated in Figs. 7.1-7.3 with the "flowing" polarization tests illustrated in Figs. 7.4-7.6. Whereas static tests often reached maximum polarizations in the range of 70-80%, the flowing tests had maximum polarizations of 20-30%. The lower polarizations during flowing tests indicated that the spin-exchange rate at the optimal temperature was still slow compared to the rate at which gas flowed through the polarization chamber. Had there been more laser power, the optimal temperature would have been higher, and the reduction in polarization during flowing conditions would have been smaller. Our initial estimates indicated that the laser power used would be close to optimal for our conditions. Our studies clearly indicate, however, that more laser power is desirable for achieving higher polarization.

A second unexpected result to come out of our research was the difference in the apparent spin-exchange rate when pumping in a field of roughly 10,000 gauss versus pumping in a field of roughly 900 gauss. While we were only in a position to measure the spin-exchange rate itself in a field of 10,120 gauss (at the center of the magnet), we were able to polarize our samples in several different fields, and measure the resulting polarization, which gave an indirect measure of the rate. In Fig. 5.5, for instance, the polarization achieved when pumping at ~900 gauss was clearly higher than that achieved at 10120 gauss despite all other conditions being quite similar. (Fig. 5.5 shows data taken under flowing conditions when the xenon was not being accumulated.) Similarly, in looking at the polarization of accumulated xenon, for various conditions as summarized in Table 5.3, it can be seen that when other factors are held constant, the better performance is associated with the lower field.

The faster spin-exchange rate of ~900 gauss is probably an indication of spin-exchange occurring due to the formation of van der Waals molecules that does not occur at the higher field of 10120 gauss. Spin-exchange in van der Waals molecules (as opposed to in binary collisions) can dominate at low pressure and low magnetic fields.

The literature clearly shows, however, that spin-exchange occurring in van der Waals molecules is suppressed as either the pressure or the magnetic field is increased. Spin exchange in binary collisions, however, is roughly independent of field and pressure. In measurements made by Cates et al. (1992), at a pressure equivalent to ours and a field of ~0.1 gauss, the spin-exchange rate was found to be ~66% due to binary collisions and ~33% due to van der Waals molecules. We would not, therefore, have expected a significant difference at the much higher fields of ~900 gauss and 10120

gauss. It is thus very helpful to have made this observation as it has important implications as we consider advanced polarizer designs.

Another goal of this research was to demonstrate that a xenon polarizer in which the polarizing chamber, accumulator and thawing all occurred in a single high-strength magnetic field would result in lower losses in the various steps and a higher final polarization. Unfortunately, the uncertainty in the calibration of the NMR in the polarization oven prevents us from quoting exact numbers for absolute losses. We were able; however, to investigate with good relative precision the effect of placing our accumulator at two different locations, one at which the field was ~10000 gauss and quite homogeneous and the other at which the field was ~2700 gauss and inhomogeneous as summarized in Table 5.3. The former resulted in around 36% higher polarization. Both this result, and the overall improved performance of our polarizer lead us to believe that there are advantages to accumulating at higher field, and further that the "single-field" approach may have advantages. The single-field approach has the disadvantage; however, that spin-exchange due to van der Waals molecules is suppressed at high field. For the future, then the lesson to be retained is probably to use high field (~10000 gauss) during accumulating and thawing. As to the relative advantages of the single-field approach, however, more study is needed.

8.2 Comparison with other designs of xenon polarizer

Prior to the beginning of this thesis project, we undertook a renovation project to improve the MITI prototype polarizer's performance. Several improvements including a new un-narrowed high power laser system, new optics, refined pumping cells, and a new magnet for the accumulator increased the ^{129}Xe polarization by roughly 5 fold.

The newly designed "2nd generation" xenon polarizer incorporated a new line-narrowed laser system, a new orthogonal laser configuration and beam-shaping optics, and a high-field single-magnet design. In the configuration tested, the 2nd generation polarizer delivered maximum polarizations that were roughly 40% higher than the maximum achieved polarizations in the upgraded MITI polarizer. Thus, the total improvement was roughly an order of magnitude compared to the performance of the MITI polarizer before the renovation project.

Specifically, we achieved maximum polarizations of thawed-out ^{129}Xe of 17.9%. Maximal polarizations as measured in the pumping chamber were 87% under static conditions and around 20-30% under flowing conditions. With 30% in the polarization chamber, a 100 minutes accumulation, and an average T_1 in the ice of 120 minutes, one would expect 20% thawed-out, reasonably close to the 17.9% measured, and probably within the relative errors between the calibrations of the two NMR systems used (The NMR system in the polarization chamber had a slightly larger uncertainty than the system used to measure the thawed-out ice.).

In placing the 2nd generation polarizer in a broader context, it is important to look both at what has been achieved, as well as what the research has taught us regarding further optimization. Already, the 2nd generation polarizer provides improved capability over what preceded it. The results of our studies clearly show; however, that additional laser power will substantially improve performance. Relatively minor changes should make it possible to continuingly deliver 350 ml quantities of xenon with polarizations over 20%. With a fully optimized system, the basic 2nd generation design should be

capable of producing 500 ml quantities with polarizations in the range of 30-40% or more.

The 2nd generation polarizer design developed in this thesis has the potential to fulfill an important niche in MR noble-gas imaging research. For groups needing 1-2 L/day of roughly 30-40% polarized xenon, our design, or a somewhat evolved version of our design, may well represent the simplest and most cost-effective approach. It is useful to compare our work with that of Ruset and Hersman et al. (2006), who designed a new xenon polarizer that operates at low gas pressure and high flow rate. They took advantage of the high spin-exchange rate constant from van der Waals collisions at low cell pressure and low magnetic field. The group reported xenon polarization of 64% at 0.3 L/hour xenon flow rate and 22% at 3 L/hour. The presumed thawed-out xenon polarization at 0.3L/hour flow rate would be ~35%-45%. Since their system operates at low gas pressure, there is no pressure broadening to increase the absorption of the laser light. The laser energy is not efficiently used. Furthermore, the gas and glassware system are more expensive, complicated and not easy for maintenance. An optimized version of the new xenon polarizer that we have developed, for quantities of 500 ml or so, should have comparable polarization for substantially less cost, while applications requiring really large amounts of gas would probably benefit from the design of Ruset and Hersman. It would appear that our approach is quite complementary in filling a niche of those requiring more limited quantities of gas.

8.3 The next step for the new xenon polarizer

It is reasonable to ask what will be the next step of this new xenon polarizer. It could be as simple as adding more laser power. Depending on the availability of laser power, more

than 20% of polarization is virtually guaranteed (we already have achieved a maximal polarization of 17.9%). A polarization range of 30%-40% appears to be a reasonable target for a fully optimized system.

Looking slightly further into the future, it is useful to consider a variant of our 2nd generation design that would be more compact and better suited to a clinical environment. Such a system could incorporate a lower field of ~20 gauss for the polarization chamber, while still maintaining a ~10000 gauss field for both accumulating and thawing the ice. With optimized laser power, such a system could be expected to reliably produce 500 ml quantities of ^{129}Xe with a polarization level of at least 30-40%.

Bibliography

Albert, M.S., Cates, G.D., Driehuys, B., Happer,W., Saam, B., Springer Jr, C.S., and Wishnia, A. (1994) Biological magnetic resonance imaging using laser-polarized ^{129}Xe. Nature 370:199-201.

Augustine, M.P., and Zilm, K.W. (1996) Optical pumping magnetic resonance in high magnetic fields: Characterization of nuclear relaxation during pumping. J. Chem. Phys. 105:2998-3011.

Augustine, M.P., and Zilm, K.W. (1996) Optical pumping magnetic resonance in high magnetic fields: characterization of the optical properties of Rb-Xe mixtures. Molecular Physics 89:737-52.

Augustine, M.P., and Zilm, K.W. (1997) Optical pumping magnetic resonance in high magnetic fields: Measurement of high field spin exchange cross sections. Chem. Phys. Lett. 280:24-30.

Bhaskar, N.D., Happer, W., Larsson, M., and Zeng, X. (1983) Slowing down of rubidium-induced nuclear spin relaxation of ^{129}Xe gas in a magnetic field. Phys. Rev. Lett. 50:105-8.

Bouchiat, M.A., Brossel, J., and Pottier, L.C. (1972) Evidence for Rb-Rare-Gas molecules from the relaxation of polarized Rb atoms in a rare gas. Experiment results. J. Chem. Phys. 56:3703-14.

Breeze, S.R., Lang, S., Moudrakovski, I., Ratcliffe, C.I., Ripmeester, J.A., Santyr, G., Simard, B., and Zuger, I. (2000) Coatings for optical pumping cells and short-term storage of hyperpolarized xenon. J. Appl. Phys. 87:8013-17.

Cates, G.D., Schaefer, S.R., and Happer, W. (1988) Relaxation of spins due to field inhomogeneities in gaseous samples at low magnetic fields and low pressures. Phys. Rev. A 37:2877-85.

Cates, G.D., Benton, D.R., Gatzke, M., Happer, W., Hasson, K.C., and Newbury, N.R. (1990) Laser production of large nuclear-spin polarization in frozen xenon. Phys. Rev. Lett. 65:2591-4.

Cates, G.D., Fitzgerald, R.J., Barton, A.S., and Bogorad, P. (1992) Rb-^{129}Xe spin-exchange rates due to binary and three-body collisions at high Xe pressures. Phys. Rev. A 45:4631-9.

Chann, B., Nelson, I., and Walker, T.G. (2000) Frequency-narrowed external-cavity diode-laser-array bar. Optics Letters 25:1352-4.

Chann, B., Nelson, I.A., Anderson, L.W., Driehuys, B., and Walker, T.G. (2002) ^{129}Xe-Xe molecular spin relaxation. Phys. Rev. Lett. 88:113201-1-4.

Chupp, T., and Swanson, S. (2001) Medical Imaging with laser polarized noble gases. Advances in atomic molecular and optical physics 45:41.

Driehuys, B., Cates, G.D., and Happer, W. (1995) Surface relaxation mechanisms of laser-polarized ^{129}Xe. Phys. Rev. Lett. 74:4943-6.

Driehuys, D., Cates, G.D., Miron, E., Sauer, K., Walter, K., and Happer, W. (1996) High-volume production of laser-polarized ^{129}Xe. Appl. Phys. Lett. 69:1668-70.

Fedchak, J.A., Cabauy, P., Cummings, W.J., Jones, C.E., and Kowalczyk, R.S. (1997) Silane coatings for laser-driven polarized hydrogen sources and targets. Nuclear Instruments and Methods in Physics Research A 391:405-16.

Fukushima, E., and Roeder, S.B.W. (1981) Experimental pulse NMR, a nuts and bolts approach. Perseus Books Publishing, L.L.C.

Gamblin, R.L., and Carver, T.R. (1965) Polarization and relaxation processes in He 3 gas. Phys. Rev. 138:A946-A960.

Jau, Y.-Y., Kuzma, N.N., and Happer, W. (2002) High-field measurement of the ^{129}Xe-Rb spin-exchange rate due to binary collisions. Phys. Rev. A 66:052710-1-7.

Killian, T. (1926) Thermionic phenomena caused by vapors of rubidium and potassium. Phys. Rev. 27:578.

Kuzma, N.N., Patton, B., Raman, K., and Happer, W. (2002) Fast nuclear spin relaxation in hyperpolarized solid ^{129}Xe. Phys.Rev. Lett. 88, 147602-1-4.

Mata, J.F., Altes, T.A., Cai, J., Ruppert, K., Mitzners, W., Hagspiel, K.D., Patel, B., Salerno, M., Brookeman, J.R., de Lange, E.E., Tobias, W.A., Wang, H.-T. J., Cates, G.D., and Mugler III, J.P. (Nov 16, 2006) Evaluation of Emphysema Severity and Progression in a Rabbit Model:A Comparison of Hyperpolarized He-3 and Xe-129 Diffusion MRI with Lung Morphometry. J. Appl. Physiol. (article in press).

Mair, R.W., Cory, D.G., Peled, S., Tseng, C.-H., Patz, S., and Walsworth, R.L. (1998) Pulsed-field-gradient measurements of time-dependent gas diffusion. J. Mag. Res. 135:478-86.

Nelson, I.A., and Walker, T.G. (2001) Rb-Xe spin relaxation in dilute Xe mixtures. Phys. Rev. A 65:012712-1-6.

Nishimura, D.G. (1996) Principles of magnetic resonance imaging. Stanford University.

Oros, A.-M., and Shah, N.J. (2004) Hyperpolarized xenon in NMR and MRI. Phys. Med. Biol. 49:R105–R153.

Ottinger, C., Scheps, R., York, G.W., and Gallagher, A. (1975) Broadening of the Rb resonance lines by the noble gases. Phys. Rev A 11:1815-1828.

Pierce Biotechonology Inc. 3747 N. Meridian Rd. P.O. Box 117, Rockford, IL 61105 www.piercenet.com

Rice, C.V., and Raftery, D. J. (2002) Rubidium-xenon spin exchange and relaxation rates measured at high pressure and high magnetic field. J. Chem. Phys. 117:5632-41.

Rohlf, J.W. (1994) Modern physics from α to Z^o. John Wiley & Sons 320-1.

Romalis, M.V., MIron E., and Cates, G.D. (1997) Pressure Broadening of Rb D1 and D2 lines by He3, He4, N_2 and Xe: line cores and near wings. Phys. Rev. A 56:P4569-78.

Rosen, M.S., Chupp, T.E., Coulter, K.P., and Welsh, R.C. (1999) Polarized ^{129}Xe optical pumping/spin exchange and delivery system for magnetic resonance spectroscopy and imaging studies. Rev. Sci. Instruments 70:1546-52.

Ruset, I.C., Ketel, S., and Hersman, F.W. (2006) Optical pumping system design for large production of hyperpolarized ^{129}Xe. Phys. Rev. Lett. 96:053002-1-4.

Salerno, M., de Lange, E.E., Altes, T.A., Truwit, J.D., Brookeman, J.R., and Mugler III, J.P. (2002) Emphysema: Hyperpolarized helium 3 diffusion MR imaging of the lungs compared with spirometric indexes—Initial experience. Radiology 222:252-60.

Shao, W., Wang, G., and Hughes, E.W. (2005) Measurement of spin-exchange rate constants between ^{129}Xe and alkali metals. Phys. Rev. A 72:022713-1-9.

Sigma-Aldrich Inc. 3050 Spruce St. St. Louis, MO 63103 www.sigmaaldrich.com

Swenson, D.R., and Anderson, L.W. (1988) Relaxation rates for optically pumped Na vapor on silicone surfaces. Nuclear Instruments and Methods in Physics Research. B29:627-42.

Tobias, W.A., Cates, G.D., Chaput, J., Deur, A., Rohrbaugh, S. and Singh, J. (2002) Application of Sol-Gel technology to high pressure polarized ^{3}He nuclear targets. Workshop on testing QCD through spin observables in nuclear targets. April 18-20, 2002, Charlottesville, VA.

Tobias, W.A. (2006) Physics, University of Virginia. Personal communication.

Tseng, C.H., Peled, S., Nascimben, L., Oteiza, E., Walsworth, R.L. and Jolesz, F.A. (1997) NMR of Laser-Polarized ^{129}Xe in Blood Foam. J. Mag. Res. 126:79-86.

Walker, T.G., and Happer, W. (1997) Spin-exchange optical pumping of noble-gas nuclei. Rev. Mod. Phys. 69:629-42.

Walsworth, R.L. et al. Group manual, Harvard University. (http://cfa-www.harvard.edu/Walsworth/pdf/OTS%20Coating%20Procedure.pdf)

Weast, R.C. editor. (1970) CRC Handbook of chemistry and physics.

Wolber, J., Cherubini, A., Leach, M.O., and Bifone, A. (2000) Hyperpolarized ^{129}Xe NMR as a Probe for Blood Oxygenation. Mag. Res. in Med. 43:491-6.

Wu., Z., Kitano., M., Happer, W., Hou, M., and Daniels, J. (1986) Optical determination of alkali metal vapor number density using Faraday rotation. Applied Optics 25:4483-92.

Zeng, X., Miron, E., van Wijngaarden, W.A., Schreiber D., and Happer, W. (1983) Wall relaxation of spin polarized 129Xe nuclei. Phy. Lett. 96A:191-4.

Zook, A.L., Adhyaru, B.B., and Bowers, C.R. (2002) High capacity production of >65% spin polarized xenon-129 for NMR spectroscopy and imaging. J. Mag. Res. 159:175-82.